Monthly Notices of the ROYAL ASTRONOMICAL SOCIETY

MNRAS **451,** 1036–1055 (2015) doi:10.1093/mnras/stv777

# Testing gravity using cosmic voids

Yan-Chuan Cai,[1,2]★ Nelson Padilla[3,4]★ and Baojiu Li[1]★

[1]*Institute for Computational Cosmology, Department of Physics, University of Durham, South Road, Durham DH1 3LE, UK*
[2]*Institute for Astronomy, University of Edinburgh, Royal Observatory, Edinburgh EH9 3HJ, UK*
[3]*Instituto de Astrofísica, Pontificia Universidad Católica de Chile, Av. Vicuña Mackenna 4860, Santiago, Chile*
[4]*Centro de Astro-Ingeniería, Pontificia Universidad Católica de Chile, Av. Vicuña Mackenna 4860, Santiago, Chile*

Accepted 2015 April 7. Received 2015 March 17; in original form 2014 October 28

## ABSTRACT

We explore voids in dark matter and halo fields from simulations of Λ cold dark matter and Hu–Sawicki $f(R)$ models. In $f(R)$ gravity, dark matter void abundances are greater than that of general relativity (GR). Differences for halo void abundances are much smaller, but still at the $2\sigma$, $6\sigma$ and $14\sigma$ level for the $f(R)$ model parameter $|f_{R0}| = 10^{-6}$, $10^{-5}$ and $10^{-4}$. Counter-intuitively, the abundance of large voids found using haloes in $f(R)$ gravity is lower, which suggests that voids are not necessarily emptier of galaxies in this model. We find the halo number density profiles of voids are not distinguishable from GR, but the same voids are emptier of dark matter in $f(R)$ gravity. This can be observed by weak gravitational lensing of voids, for which the combination of a spec-$z$ and a photo-$z$ survey over the same sky is necessary. For a volume of 1 (Gpc $h^{-1}$)$^3$, $|f_{R0}| = 10^{-5}$ and $10^{-4}$ may be distinguished from GR at $4\sigma$ and $8\sigma$ using the lensing tangential shear signal around voids. Sample variance and line-of-sight projection effect sets limits for constraining $|f_{R0}| = 10^{-6}$. This might be overcome with a larger volume. The smaller halo void abundance and the stronger lensing shear signal of voids in $f(R)$ models may be combined to break the degeneracy between $|f_{R0}|$ and $\sigma_8$. The outflow of dark matter from void centres are 5, 15 and 35 per cent faster in $f(R)$ gravity for $|f_{R0}| = 10^{-6}$, $10^{-5}$ and $10^{-4}$. The velocity dispersions are greater than that in GR by similar amounts. Model differences in velocities imply potential powerful constraints for the model in phase space and in redshift space.

**Key words:** gravitational lensing: weak – methods: statistical – large-scale structure of Universe.

## 1 INTRODUCTION

Cosmic voids as cosmological probes have been explored in many aspects. For example, the Alcock–Paczynski test using stacking of voids has been demonstrated to be a powerful probe of distance distortions between the line of sight and transverse directions (Lavaux & Wandelt 2012; Sutter et al. 2014a); stacking of voids for the cosmic microwave background has been used as an alternative to the cross-correlation method to detect the integrated Sachs–Wolfe effect (Granett, Neyrinck & Szapudi 2008; Cai et al. 2013, 2014; Ilić, Langer & Douspis 2013; Planck Collaboration XIX 2014; Hotchkiss et al. 2015); the weak gravitational lensing effect of voids, as an analogue to that of haloes, has been shown to be capable of measuring the matter density profiles of voids (Clampitt & Jain 2014; Melchior et al. 2014); void ellipticity has been shown to be sensitive to the dark energy equation of state (Bos et al. 2012); void properties have been studied in dynamical dark energy (Bos et al. 2012), coupled dark energy (Li 2011; Sutter et al. 2015) and modified gravity (Li, Zhao & Koyama 2012b) models using $N$-body simulations.

The basic properties of voids – their abundances and density profiles – can be powerful in constraining theories of cosmology and gravity, but there are still gaps between observations and theoretical predictions for these two properties. The reasons are partly related to the technical details of how voids are defined: (1) given the same simulation, different void-finding algorithms do not usually find the same voids (Colberg et al. 2008); (2) voids defined using tracers (galaxies or haloes) are expected to be different from voids defined using the dark matter field. Nevertheless, studies of void profiles have made encouraging progress in the last decades. Applying a spherical underdensity algorithm to find voids in $N$-body simulations, Colberg et al. (2005) have found that void profiles are self-similar within the effective void radius they defined, (but see Ricciardelli, Quilis & Varela 2014). Using ZOBOV (Neyrinck, Gnedin & Hamilton 2005), Hamaus, Sutter & Wandelt (2014) have found that dark matter void profiles within a wide range of radii can be similar if rescaled using two free parameters. Using mocks and real Luminous Red Galaxies (LRG) galaxies from Sloan Digital

★ E-mail: cai@roe.ac.uk (Y-CC); npadilla@astro.puc.cl (NP); baojiu.li@durham.ac.uk (BL)

Sky Survey (SDSS), Nadathur et al. (2015) found an even simpler rescaling relationship among voids of different sizes, using only one parameter.

It is perhaps more challenging to use void abundance to constrain cosmology. Excursion set theory offers predictions of the void abundance but the agreement with $N$-body simulations is never as great as in the case of haloes (Sheth & van de Weygaert 2004; Colberg et al. 2005; Paranjape, Lam & Sheth 2011; Achitouv, Neyrinck & Paranjape 2013). A recent attempt to compare void abundance between simulations and excursion set theory has found that they may agree at $\sim$16 per cent at $z = 0$ if dark matter is used to define voids in simulations (Jennings, Li & Hu 2013), but the agreement is much worse if haloes are used instead. It would be even harder to compare theoretical predictions with observed void abundances from galaxy surveys due to the systematics introduced by survey geometry and masks. One possible way to overcome this is to apply the same algorithm to simulations and observations, which makes comparisons of void properties with simulations meaningful.

In this work, we will focus on the potential of using the above two basic properties of voids to constrain modified gravity. Scalar-field models of modified gravity could drive the late-time accelerated expansion of the Universe without explicitly invoking a cosmological constant. Although such theories often introduce extra long-range forces (known as fifth forces) mediated by the scalar fields, they can still in principle pass local tests of gravity via certain screening mechanisms, such as the Vainshtein (Vainshtein 1972) or chameleon (Khoury & Weltman 2004) mechanisms. More explicitly, the success of those models largely relies on the screening mechanism to suppress the fifth force in overdense regions, where most of current astronomical observables come from. It is therefore inbuilt in these models that their differences from general relativity (GR) are minimal in high-density environments like dark matter haloes, galaxies and the local Solar system. Nevertheless, in these models, the growth of structure is altered to some extent due to the coupling of scalar fields with matter, though the ensemble average of the growth at large scales might still be the same as in $\Lambda$ cold dark matter ($\Lambda$CDM; Jennings et al. 2012; Li et al. 2013). For example, in $f(R)$ (Hu & Sawicki 2007), which is mathematically equivalent to the coupled scalar field model mentioned above, the difference from $\Lambda$CDM in terms of the halo mass function and matter power spectrum may not be in obvious contradiction with observational data (see below). It is therefore interesting and necessary to explore alternative probes that are sensitive to the environment-dependent nature of these models.

Voids in modified gravity have previously been studied by Li et al. (2012b) using $N$-body simulations, and by Martino & Sheth (2009), Clampitt, Cai & Li (2013) and Lam et al. (2015) using analytical methods. For chameleon-type coupled scalar field models, the fifth force is found to counter the standard Newtonian gravity in underdensities (Clampitt et al. 2013). The repulsive force drives underdensities to expand faster and grow larger, hence also changing the distribution and abundances of voids. This naturally implies that the two basic properties of voids, their density profiles and abundances, can be promising tools to probe and constrain modified gravity.

In this work, we use a set of $N$-body simulations of the $f(R)$ model to study properties of voids in detail, focusing on prospective observables to distinguish the $f(R)$ model from GR using voids. In Section 2, the basics of the $f(R)$ models and the $N$-body simulations are introduced. Section 3 summarizes our void-finding algorithm. We present the main results of comparing void properties, and discuss the observational implications in Sections 4 and 5.

## 2 THE $f(R)$ GRAVITY MODEL AND ITS SIMULATIONS

In this section, we briefly describe $f(R)$ gravity and its simulations. Readers familiar with its content can simply skip this section.

### 2.1 The $f(R)$ gravity model

The $f(R)$ gravity model (Carroll et al. 2005) generalizes GR by simply replacing the Ricci scalar $R$ in the standard Einstein–Hilbert action by an algebraic function $f(R)$ (see e.g. De Felice & Tsujikawa 2010; Sotiriou & Faraoni 2010, for some recent reviews):

$$S = \frac{M_{\rm Pl}^2}{2}\int \mathrm{d}^4x\sqrt{-g}\,[R + f(R)]\,, \tag{1}$$

where $M_{\rm Pl}$ is the reduced Planck mass, which is related to Newton's constant $G$ by $M_{\rm Pl}^{-2} = 8\pi G$, and $g$ is the determinant of the metric tensor $g_{\mu\nu}$.

In $f(R)$ gravity, the quantity $f_R \equiv \mathrm{d}f/\mathrm{d}R$ behaves as a scalar field and mediates an extra force, often called the fifth force. Often, the fifth force is taken as part of the total gravity, which is one reason why $f(R)$ gravity is a modified gravity model. Hence, we need to understand the dynamics of both the Newtonian potential $\Phi$ and $f_R$.

The detailed derivation of the field equations in $f(R)$ gravity can be found in the literature (see e.g. Cai et al. 2014), and will not be repeated here. In this paper, we are interested in the formation of large-scale structures on scales substantially below the horizon, and the time variation of $f_R$ is small in the models we will consider (Bose, Hellwing & Li 2015). Therefore, we will work with the quasi-static approximation by neglecting the time derivatives of $f_R$ in all field equations. Under this approximation, $f_R$ depends on the matter density $\rho_{\rm m}$ through

$$\nabla^2 f_R = -\frac{1}{3}a^2\left[R(f_R) - \bar{R} + 8\pi G\left(\rho_{\rm m} - \bar{\rho}_{\rm m}\right)\right], \tag{2}$$

in which $\nabla$ is the three-dimensional gradient operator, and the overbar takes the background averaged value of the quantity under it. Note that $R$ has been expressed as a function of $f_R$ by reverting $f_R(R)$. $a$ is the cosmic scale factor normalized to $a = 1$ today. Meanwhile, the Poisson equation for the Newtonian potential $\Phi$ is modified as

$$\nabla^2\Phi = \frac{16\pi G}{3}a^2\left(\rho_{\rm m} - \bar{\rho}_{\rm m}\right) + \frac{1}{6}a^2\left[R\left(f_R\right) - \bar{R}\right]. \tag{3}$$

There are two different regimes of solutions to the above equations. When $|f_R| \ll |\Phi|$, equation (2) gives $R \approx -8\pi G\rho_{\rm m}$ and equation (3) reduces to the normal Poisson equation of GR:

$$\nabla^2\Phi = 4\pi G a^2\left(\rho_{\rm m} - \bar{\rho}_{\rm m}\right). \tag{4}$$

This is the screened regime, where the fifth force is suppressed by the chameleon mechanism (Khoury & Weltman 2004), so named because it works in regions with deep $|\Phi|$. For an $f(R)$ model to be viable, our Solar system needs to be in this regime.

In contrast, for $|f_R| \gtrsim |\Phi|$, we have $|R - \bar{R}| \ll 8\pi G|\rho_{\rm m} - \bar{\rho}_{\rm m}|$ and then equation (3) reduces to

$$\nabla^2\Phi = \frac{16\pi G}{3}a^2\left(\rho_{\rm m} - \bar{\rho}_{\rm m}\right). \tag{5}$$

This is the unscreened regime, where the total gravity is enhanced by a maximal factor of 1/3 compared with GR, independent of the functional form of $f(R)$. This occurs mostly in low-density regions such as on the cosmological background, which means that an $f(R)$ model can behave very differently on cosmological scales even if it goes back to GR locally.

### 2.2 The Hu–Sawicki model

In this paper, we will focus on the $f(R)$ model proposed by Hu & Sawicki (2007), which is specified by

$$f(R) = -M^2 \frac{c_1(-R/M^2)^n}{c_2(-R/M^2)^n + 1}, \tag{6}$$

where $c_1$, $c_2$ are dimensionless parameters, $M^2 \equiv 8\pi G\bar{\rho}_{\rm m0}/3 = H_0^2\Omega_{\rm m}$ is a new mass scale, with $H$ the Hubble expansion rate and $\Omega_{\rm m}$ the present-day fractional energy density of matter. Hereafter, a subscript $_0$ denotes the present-day value of a quantity.

At the cosmological background level, if $|\bar{R}| \gg M^2$, then the modified Einstein equation in this model can be approximated as

$$-\bar{R} \approx 8\pi G\bar{\rho}_{\rm m} - 2\bar{f} \approx 3M^2\left(a^{-3} + \frac{2c_1}{3c_2}\right). \tag{7}$$

Therefore, to reproduce approximately the background expansion history of a ΛCDM model, we simply set

$$\frac{c_1}{c_2} = 6\frac{\Omega_\Lambda}{\Omega_{\rm m}}, \tag{8}$$

where $\Omega_\Lambda = 1 - \Omega_{\rm m}$ is the present-day fractional energy density of the cosmological constant.

By taking $\Omega_\Lambda = 0.76$ and $\Omega_{\rm m} = 0.24$, we find that $|\bar{R}| \approx 41M^2 \gg M^2$ today ($|\bar{R}|$ is even larger at earlier times), and this simplifies the expression of $f_R$ to

$$f_R \approx -n\frac{c_1}{c_2^2}\left(\frac{M^2}{-R}\right)^{n+1} < 0. \tag{9}$$

As only $f_R$ enters equations (2) and (3), the two free parameters $n$ and $c_1/c_2^2$ completely specify this $f(R)$ model, and we have

$$\frac{c_1}{c_2^2} = -\frac{1}{n}\left[3\left(1 + 4\frac{\Omega_\Lambda}{\Omega_{\rm m}}\right)\right]^{n+1} f_{R0}. \tag{10}$$

In this paper, we will study three $f(R)$ models with $n = 1$ and $|f_{R0}| = 10^{-6}$, $10^{-5}$, $10^{-4}$, which will be referred to as F6, F5 and F4, respectively. These choices of $|f_{R0}|$ are designed to cover the part of the parameter space which is cosmologically interesting: if $|f_{R0}| > 10^{-4}$ then the $f(R)$ model violates the cluster abundance constraints (Schmidt, Vikhlinin & Hu 2009), and if $|f_{R0}| < 10^{-6}$ then the model is too close to ΛCDM to be distinguishable in cosmology. Lombriser (2014) gives an excellent review on the current cosmological and astrophysical constraints on $f_{R0}$.

### 2.3 *N*-body simulations of $f(R)$ gravity

The simulations used for the analyses in this work were ran using the ECOSMOG code (Li et al. 2012a), and are listed in Table 1. They all have the same values of cosmological parameters, summarized here as $\Omega_{\rm m} = 0.24$, $\Omega_\Lambda = 0.76$, $h = 0.73$, $n_{\rm s} = 0.958$ and $\sigma_8 = 0.80$, in which $h \equiv H_0/(100\ {\rm km\ s^{-1}\ Mpc^{-1}})$, $n_{\rm s}$ is the spectral index of the scalar primordial power spectrum and $\sigma_8$ is the linear rms density fluctuation measured in spheres of radius 8 Mpc $h^{-1}$ at $z = 0$. For comparisons, we ran both $f(R)$ and GR simulations, and used ΛCDM background evolution history in all our simulations.

We call a group of ΛCDM, F6, F5 and F4 simulations with the same technical settings (e.g. box size and resolution) a simulation suite. All models in each simulation suite share the same initial condition generated using the Zel'dovich approximation at an initial redshift, $z_i = 49$. Although generally speaking the modified gravitational law also affects the generation of the initial condition (Li & Barrow 2011), in the $f(R)$ models studied here the fifth force is strongly suppressed at $z_i \geq$ a few, and so its effects are negligible at the initial times. Hence, the initial density fields for the ΛCDM and $f(R)$ simulations share the same phases, and any difference in the void properties that we find at late times is a direct consequence of the different dynamics and clustering properties of these models.

## 3 VOID FINDING ALGORITHM

We use a void finder based on the one presented by Padilla, Ceccarelli & Lambas (2005, hereafter P05) with improvements centred on optimizing the method, on improving its convergence for different mass resolutions and box sizes, and adapted to run on parallel computers. Our finder can be run either on the dark matter field or using dark matter halo tracers.

In the case of searching for voids in the dark matter field, the improved finder (iP05 from now on) follows the following steps.

(i) It searches throughout the simulation volume for regions of low density, performing a top-hat smoothing of the density field on a grid. We take all the grid cells with a density below a set threshold $\delta_{\rm cell}$ as prospective void centres. We define a grid such that each cell contains on average 10 dark matter particles so as to avoid being affected by shot noise that unnecessarily increases the number of prospective centres when this minimum number is lower. In the case when the detection of voids is done using haloes, we adopt the same average number of objects in a cell (notice that since haloes trace peaks of the dark matter field, this is probably a conservative choice). We adopt a grid threshold $\delta_{\rm cell} = -0.9$, i.e. only empty cells are prospective void centres.

(ii) We start measuring the underdensity in spheres of increasing radius about these centres until some void threshold, $\Delta_{\rm void}$, is reached. If the largest sphere about any one centre contains at least 20 particles, it is kept as a void candidate. This number provides the best stability of the method against resolution and boxsize changes when searching for voids in the dark matter density field. In almost all cases, we adopt a value of $\Delta_{\rm void} = -0.8$. However, for $z > 0$ we also adopt different thresholds that take into account the linear growth of perturbations until $z = 0$ (this will be indicated for each particular case). The void radius is defined as the radius of the underdense sphere. As a result, the void density profiles typically reach the cosmic mean density quite farther from the void radii.

**Table 1.** Some technical details of the simulations performed for this work. F6, F5 and F4 are the labels of the Hu–Sawicki $f(R)$ models with $n = 1$ and $|f_{R0}| = 10^{-6}$, $10^{-5}$, $10^{-4}$, respectively. Here, $k_{\rm Nyq}$ denotes the Nyquist frequency. The last column lists the number of realizations for each simulation.

| Models | $L_{\rm box}$ | Number of particles | $k_{\rm Nyq}$ ($h$ Mpc$^{-1}$) | Force resolution ($h^{-1}$ kpc) | number of realizations |
|---|---|---|---|---|---|
| ΛCDM, F6, F5, F4 | 1.5 $h^{-1}$ Gpc | $1024^3$ | 2.14 | 22.9 | 6 |
| ΛCDM, F6, F5, F4 | 1.0 $h^{-1}$ Gpc | $1024^3$ | 3.21 | 15.26 | 1 |
| ΛCDM | 250 Mpc $h^{-1}$ | $1024^3$ | 12.82 | 3.8 | 1 |

(iii) The candidates are ranked in decreasing order of size, and we reject all spheres which overlap with a neighbouring sphere with a larger radius by more than a given percentage of the sum of their radii. This percentage will be treated as a free parameter: increasing the overlap percentage increases the size of the sample, which helps to obtain better statistics, but it also introduces larger covariances in the results, which could in the end lower the significance of a comparison between models. In the case of voids in the distribution of the dark matter field, we choose to use 10 per cent overlap.

Following Ceccarelli et al. (2013), voids are classified into void-in-void and void-in-cloud objects depending on whether the accumulated overdensity at three void radii from the void centre is below or above zero, respectively, or simply by dividing our sample in different void sizes, since smaller voids contain larger fractions of void-in-cloud objects (see Cai et al. 2013; Ceccarelli et al. 2013; Hamaus et al. 2014, for examples).

When searching for voids in the distribution of dark matter haloes, step (ii) above is slightly modified, where we now do not demand a minimum number of haloes within a void. This is due to the high significance of the peaks marked by haloes, which implies that a volume empty of haloes is one with no peaks, and as such it is of interest to us. Furthermore, if for the same initial conditions the resolution of the simulation were improved, the haloes of the lower resolution simulation would again be found, though the dark matter particle positions would indeed change due to the change in the sampling of the smooth density field. Additionally, we will allow the percentage of void overlapping to vary from 50 to 0, in order to search for the optimal sample to distinguish between GR and $f(R)$ models.

Using haloes to identify voids is more practical observationally than using dark matter, but one has to face the challenge of sparse sampling. Especially, the centring of the spherical voids needs to be done more carefully since haloes only sparsely sample the density field. In particular, since a sphere can be defined by four points on its surface, a well-centred spherical void should contain four haloes, all living at a distance of exactly one void radius from the void centre. However, the precision of centring of our voids is of 0.3 Mpc $h^{-1}$, so we do expect some dispersion in the distance to the first four closest haloes. We assess the quality of our voids using this dispersion defined as

$$\sigma_4 \equiv \sqrt{\left\langle \left( \frac{d_i - \langle d_i \rangle_4}{\langle d_i \rangle_4} \right)^2 \right\rangle_4}, \tag{11}$$

in which $d_i$ is the distance from the void centre to the $i$th halo, and $\langle\rangle_4$ denotes the average over the 4 closest haloes. The typical value for this parameter in our void samples is $\sigma_4 \simeq 0.05$, as shown in the inset of Fig. 5.

When using haloes as tracers, our void finder identifies voids with no haloes, but also allows voids to contain one or more haloes within its volume, as long as the threshold criterion, $\Delta_{\rm void} = -0.8$, is met. Note that we have $\Delta_{\rm void} = \delta n/\bar{n}$ when referring to threshold criterion for halo-identified voids, where $n$ is the halo number density; in contrast, for voids identified using the dark matter field, the threshold is defined as $\Delta_{\rm void} = \delta\rho_{\rm m}/\bar{\rho}_{\rm m}$.

There are several routes to come closer to voids as would be identified with real galaxy catalogues. For example, one could simply weight each dark matter halo by the halo occupation number that corresponds to its mass. To do this, though, one needs the halo occupation distribution (HOD) parameters fit to observational data, and this is currently only available for ΛCDM (e.g. Zehavi et al. 2011). In order to make a consistent comparison between GR and $f(R)$ gravity it would be necessary to first find the HOD parameters for the $f(R)$ cosmologies. Another possible avenue is to use semi-analytic galaxies, obtained by coupling a semi-analytic galaxy formation model to the merger trees extracted from the GR and $f(R)$ simulations. This approach is again not ideal because it assumes that the physics of galaxy formation is the same in both models, which may not be the case. Our present approach of using haloes as tracers is comparable to identifying voids in galaxy group catalogues, and as such is already applicable to current surveys.

## 4 VOID ABUNDANCE

We have discussed that voids can be identified using either the dark matter field or biased tracers such as dark matter haloes or galaxies. Although the latter are more directly related to real observational data, the former is of more theoretical interest, as it directly reflects how dark matter clusters under the action of modified gravitational laws. In this section, we show void abundances found in both ways.

### 4.1 Voids identified using the dark matter field

We use the iP05 finder on the dark matter field of the 1000 Mpc $h^{-1}$ a side boxes for the GR, F6, F5 and F4 simulations. The resulting abundances as a function of void radius are shown in Fig. 1. We show the results for the voids identified using positions in real space for the dark matter particles. In order to determine the minimum void radius above which our void sample is complete in these simulations, we run the void finder in smaller 250 Mpc $h^{-1}$ simulations with the same number of particles, i.e. with 64 times the mass resolution, and find that the abundances of the small and large simulations are

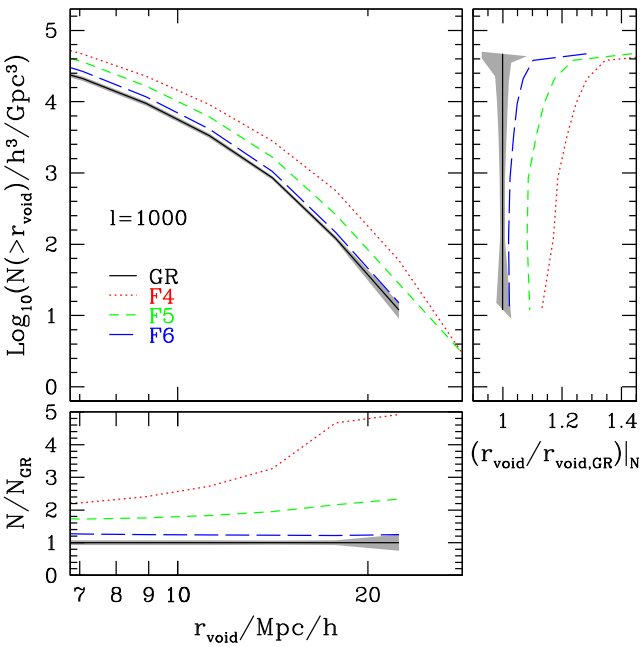


**Figure 1.** Void abundance as a function of void radius in real space, for the GR, F6, F5 and F4 simulations of 1000 Mpc $h^{-1}$ a side boxes (different line types indicated in the key). The shaded region shows the errors obtained from multiple realizations of a larger simulation. The lower sub-panel shows the abundance ratio between the different models and GR, while the right sub-panel shows the ratios between void radii at fixed abundances with respect to GR, with the aim to show whether the shape of the distributions are similar or not; if so this ratio would appear as a straight vertical line.

consistent down to a void radius of 7 Mpc $h^{-1}$. Therefore, from this point on, we will concentrate on voids of at least this size unless otherwise stated.

As can be seen in the main panel of Fig. 1, the abundance of voids at a fixed radius increases from GR to $f(R)$ gravity, as expected due to the action of the fifth force that tends to point towards the void walls (Clampitt et al. 2013), which is stronger progressing from F6 through F5 to F4. Dark matter voids in $f(R)$ models therefore grow larger and their abundances greater.

The lower sub-panel shows the ratios of the abundances of the modified gravity models with respect to GR. The F4 model shows the strongest differences from GR, with abundances higher by factors of ∼1–4, and larger for larger void radii. One question that remains open is whether the increase in abundance corresponds solely to an increase in void radius by a factor independent of void size. If this were the case, then the functions would maintain their shapes and only shift to the right by a constant factor. In order to check this, the right sub-panel shows the ratio of void sizes at fixed void number densities, where the roughly constant ratios (close to vertical straight lines) indicate that the differences between the models are almost due to larger void sizes for the modified gravity models compared with GR. Only at high number densities (high $y$-axis values) the ratios start to increase steadily (lines curving towards the right) indicating a slight increase of abundance for small voids in $f(R)$ models with respect to GR. We checked the results in redshift space and found very small differences from what is shown in Fig. 1.

The shaded region in Fig. 1 shows the error in the GR abundances, and the lower panel shows that the GR and F6 abundances are significantly different, by at least three standard deviations ($3\sigma$) up to void radii $\simeq 20$ Mpc $h^{-1}$. To estimate these, we have used larger simulations of 1500 Mpc $h^{-1}$ a side, for which there are a total of six realizations for each model. In order to estimate errors for the cubic gigaparsec simulations, we simply compute the dispersion of abundances measured in 1000 Mpc $h^{-1}$a side sub-boxes of the large simulations (simply taking one sub-volume per box starting from the (0, 0, 0) coordinates). We use these errors instead of Poisson estimates since the dispersion from multiple realizations is more representative of the cosmic variance. Fig. 2 shows different estimates of cumulative abundance errors for the GR (solid) and F4 (dotted lines) models for the large simulations. The black lines correspond to the Poisson estimates of the errors and the red lines to the dispersion of the different realizations using the full simulation volume. These two estimates of errors are very different for void radii <20 Mpc $h^{-1}$; this is the reason why we adopt the realization dispersion. The other lines show the dispersion of 1000 (blue) and 250 Mpc $h^{-1}$ (green) a side sub-boxes. As can be seen, decreasing the volume to 1(Gpc $h^{-1}$)$^3$ does not increase the errors as it would be expected from Poisson fluctuations. The errors for the smaller volume of 250 Mpc $h^{-1}$ are much larger, on the other hand.

As mentioned in the introduction, the main motivation to study voids in modified gravity models is that the abundances of voids are more sensitive to the fifth force than the halo mass functions. The latter is shown in Fig. 3, where it can be seen that the change of the halo abundance as we move from GR through F6 and F5 to F4 is complicated. Furthermore, the F6 model shows virtually no differences from the GR abundances down to masses $\simeq 10^{14}\ h^{-1}\,\mathrm{M}_\odot$, whereas the void abundance is significantly different between these two models across the range of void sizes reliably accessible in our simulations. The dark matter haloes are identified using the spherical overdensity code AHF (Knollmann & Knebe 2009).

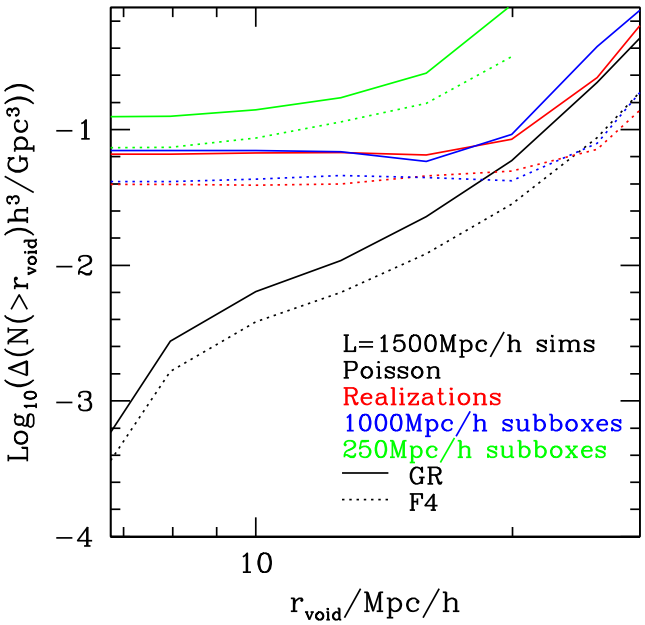


**Figure 2.** Void abundance errors obtained from six realizations of our 1500 Mpc $h^{-1}$ a side simulations. We show errors arising from assuming Poisson fluctuations (black), the dispersion from the realizations for the full simulation volumes (red), and for two smaller sub-volumes (blue and green), for the GR and F4 models (solid and dotted, respectively).

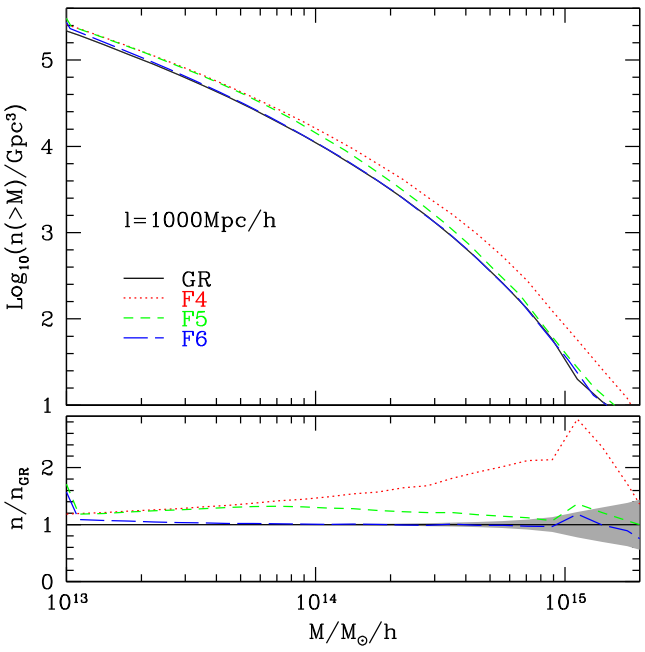


**Figure 3.** Cumulative halo mass functions for the GR, F6, F5 and F4 models (different line types and colours as indicated in the key). The shaded area shows the Poisson error in the GR model. The lower panel shows the ratio between the different $f(R)$ models and GR, using the same colours as in the top panel.

Given that large galaxy surveys are getting deeper, we also measure the abundance of voids at two higher redshifts, $z = 0.43$ and 1. Since fluctuations grow with time one can either use a fixed density threshold to identify voids at different redshifts, or make it evolve with the growth of fluctuations. We adopt both approaches and show

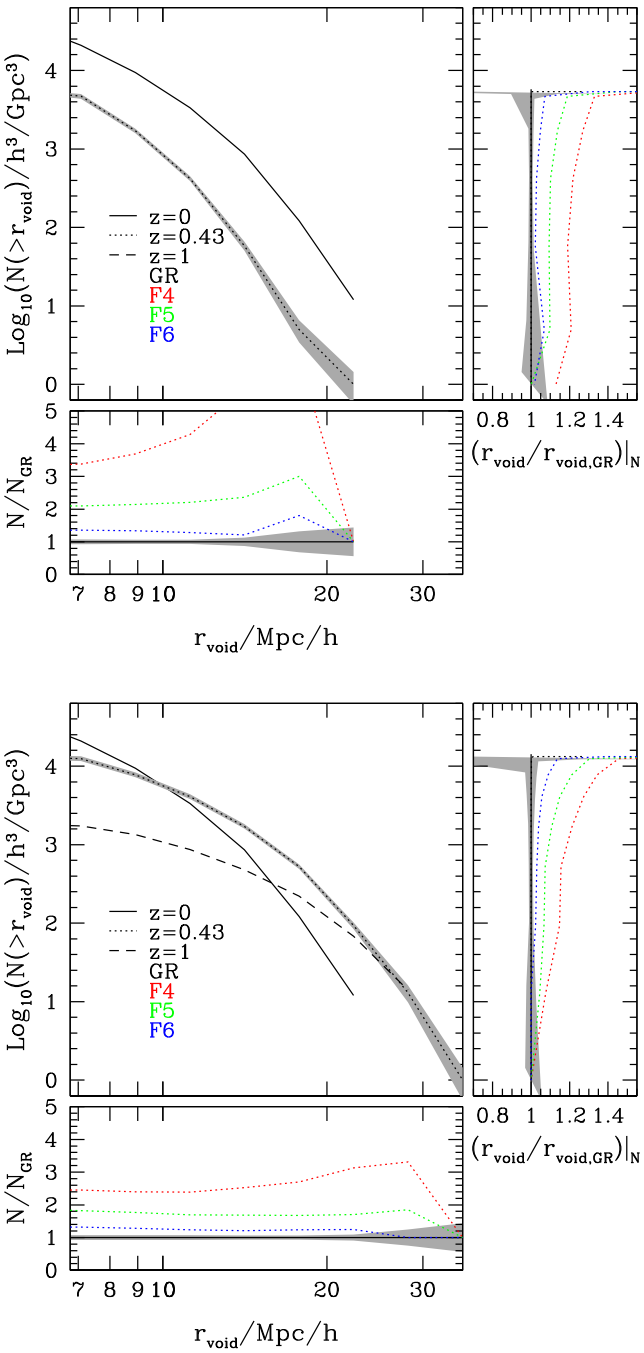


**Figure 4.** Void abundances at different redshifts (solid, dotted and dashed as the redshift increases), adopting the same overdensity threshold of $\Delta_{\rm void} = -0.8$ (top panels), and a threshold which evolves according to the linear perturbation growth, $\Delta_{\rm void} = -0.8$, $-0.65$ and $-0.51$ for $z = 0$, 0.43 and 1.0, respectively (bottom panels). For clarity, the main panels only show the results for the GR simulation. The lower sub-panels are as in Fig. 1, showing the relative changes in abundance with respect to GR for $z = 0.43$ only for clarity. The right sub-panels show the ratio between $f(R)$ void radii with respect to GR values at fixed abundance, for voids at $z = 0.43$. A vertical line would indicate a shift by a constant factor in void radius alone. The shaded areas show the errors, which are for GR only at $z = 0.43$ for clarity.

the results in Fig. 4, where the top panels show the results for a fixed threshold of $\Delta_{\rm void} = -0.8$, and the bottom panels for an evolving threshold following the linear growth of fluctuations for the cosmology of the GR simulation (differences are almost indistinguishable for the modified gravity models adopted here), with $\Delta_{\rm void} = -0.8$, $-0.65$ and $-0.51$ for $z = 0$, 0.43 and 1.0, respectively. To improve clarity the main panels only show the results for the GR simulations, but the lower sub-panels show the ratio of abundances with respect to GR (colours for different models) for $z = 0.43$. The right sub-panels show the ratio between void sizes at fixed abundance at $z = 0.43$, with respect to GR. Comparing to the right-hand panel of Fig. 1, the difference between $f(R)$ gravity and GR in terms of void abundance is not strongly dependent on redshift or on the density contrast adopted to identify the voids. For both cases, there are changes in the shape of the distribution functions, which tend to increase more in $f(R)$ at small void radii.

The main panels of Fig. 4 show that a fixed threshold effectively produces much smaller samples at $z = 0.43$ and 1, to the point that for the latter the number of voids is too small to appear in the figure. This is because very empty regions, e.g. $\Delta_{\rm void} \leq -0.8$, only form at late times. An evolving threshold, on the other hand, produces higher abundances of large (comoving size) voids, but a smaller total number of voids (the intersection of the lines with the $y$-axis). This may be due to the use of linear theory to rescale the threshold, which is likely to be overevolving the actual growth of fluctuations because the evolution of underdensities tends to be slower than the linear theory result. We have found that the main difference in the abundance of voids for a fixed threshold can be absorbed by a constant factor in the void radius: $z = 0.43$ voids are $\simeq 0.7$ times smaller than those at $z = 0$, whereas $z = 1$ voids are $\sim$5 times smaller than at $z = 0$. The constant shifts of the void abundance functions among different epochs reflect a simple picture for the evolution of voids, which is captured by our void algorithm. More in-depth study of the evolution of void abundance is needed to shed light on the physics behind this behaviour.

Regarding the differences between $f(R)$ gravity and GR, at higher redshifts the abundances are higher in the F6 to F4 models with respect to GR, by factors similar to those at $z = 0$ (see the lower sub-panels). However, if a fixed density threshold is adopted, the number of voids will be smaller and the errors larger, making the difference between F6 and GR less significant. This should not be a problem if the evolving threshold is adopted. The errors shown in the figure correspond to $z = 0.43$, which are similar to those shown in Fig. 1 for the evolving threshold case. We find that for the volume of our simulations, the errors depend mostly on the number of voids – although in a way that differs from Poisson statistics as shown above – and therefore only the fixed threshold case shows larger errors at higher redshifts as the numbers of voids are smaller.

### 4.2 Voids identified using dark matter haloes

In real observations, voids are usually identified by using tracers of large-scale structure, such as galaxies. In general, to compare simulations with observational data, one has to generate galaxy mocks. However, P05 has shown that the properties of voids found from mock galaxies are compatible with those of voids identified from dark matter haloes. Also, as mentioned above, the use of HOD or semi-analytic galaxy mocks incur further complications in the framework of $f(R)$ gravity, the remedy of which is beyond the scope of the present work. Therefore, as an initial step, we only use voids found using dark matter haloes.

We apply our void-finding algorithm to the halo field in our simulations of GR and $f(R)$ gravity. We use haloes with the mass cutoffs $M_{\rm min} = 10^{12.8}$, $10^{12.868}$, $10^{12.865}$ and $10^{12.842}\,{\rm M}_\odot\,h^{-1}$ for GR, F4, F5 and F6 simulations, respectively, where $M_{\rm min}$ is the minimal halo mass of the catalogue. $M_{\rm min}$ is chosen to ensure that the haloes

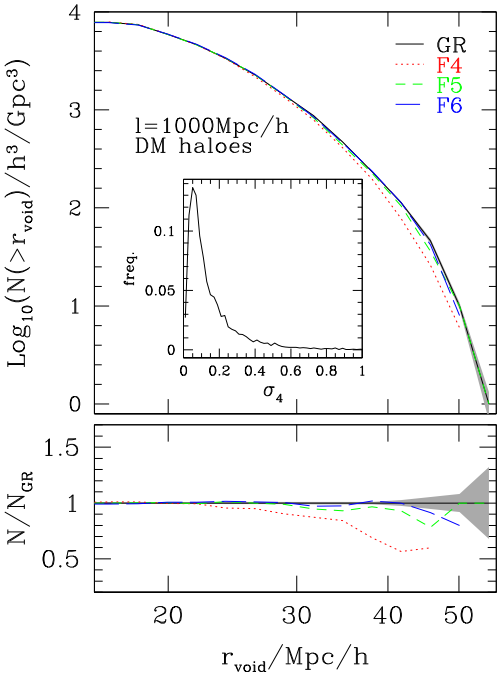


**Figure 5.** Void abundances from using dark matter haloes as tracers of the density field. Lines and lower sub-panel are as in Fig. 1. The inset in the main panel shows the distribution function of $\sigma_4$, the relative dispersion in the distance to the first four haloes above the void density threshold, for GR; a small value of $\sigma_4$ indicates a well centred void.

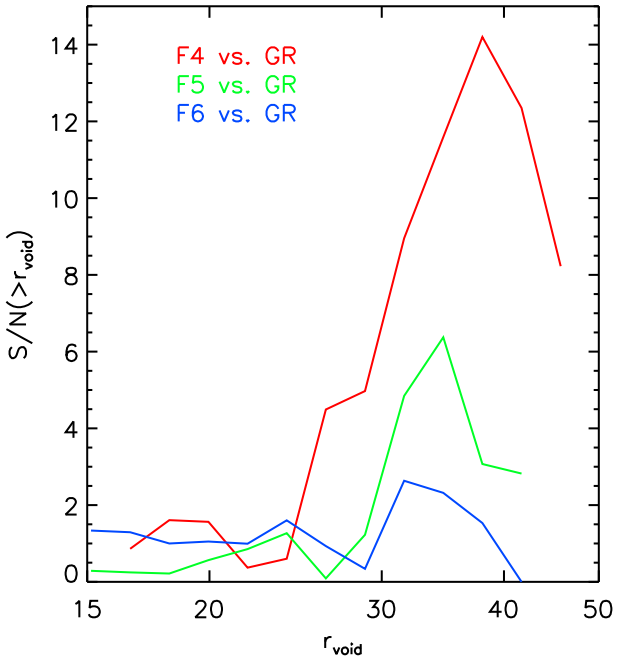


**Figure 6.** The corresponding S/N from void abundances shown in Fig. 5.

contain at least 100 particles each, and the slight differences in the $M_{\rm min}$ values for different models is to make sure that the halo number densities among different models are the same. This is necessary because it is likely that different populations of voids will be found if the tracer densities are different, even for the same simulations. By using the same number densities of tracers for different models, we minimize the impact of tracers on void populations of different models, and it is observationally meaningful as we only need to require having the same galaxy number density from observations. As mentioned in the previous section, we explore the results in the halo defined void statistics using different overlap percentages of 50 to 0, and study the effects this choice has on the significance of the comparison between GR and $f(R)$ statistics.

The resulting void abundances for halo voids with 20 per cent overlap are shown in Fig. 5. The results have several important features. First, since haloes are highly biased tracers of dark matter, and are mainly distributed along walls and filaments, voids found in this way are more abundant and larger than those identified from the dark matter field. Secondly, the differences of the void abundances among different models are much smaller than in the case of dark matter voids, though they are still significant as shown in Fig. 6. The relatively small differences in halo void abundances are possibly a consequence of the fact that haloes are highly biased tracers of the underlying dark matter field and have formed from the high peaks of the initial density field: while the fifth force can drastically change the clustering of dark matter, its effects on haloes are weaker and a density peak which corresponds to a halo in $f(R)$ simulations is also likely to have formed a halo in the GR simulation. Thirdly, and most interestingly, we notice that voids larger than $r_{\rm void} \simeq 25$ Mpc $h^{-1}$ are less abundant in $f(R)$ models than in GR.

The lower abundance of voids with $r_{\rm void} \geq 25$Mpc $h^{-1}$ in $f(R)$ is counter intuitive and may seem inconsistent with the physical picture that voids grow larger and emptier in $f(R)$ gravity because the fifth force points towards the edges of voids (Clampitt et al. 2013). To check this, we use the void centres found in the GR simulation and count all the haloes residing within the GR void radius, for the different models. Two examples comparing F4 and GR halo number counts in this way are presented in Fig. 7. It is interesting to note that there are more haloes found in the $f(R)$ simulation within the same void radii, even when the minimal halo mass cut is lower for GR (as indicated by the dotted lines). This is likely due to the stronger environmental dependence of halo formation in $f(R)$ models (Li & Efstathiou 2012). The fifth force in $f(R)$ gravity in these large underdense environments is stronger, which makes it more likely for haloes of the same mass to form in $f(R)$ than in GR. The halo number density within the same sphere is therefore smaller in GR than in $f(R)$, making it easier to pass our void selection criteria in the former case. We can also see that the masses of haloes in F4 are larger. Thus, even if we make the same $M_{\rm min}$ cuts for both simulations, the same phenomenon that the largest voids in GR are bigger than in $f(R)$ gravity would still be present, as we have checked explicitly.

At the largest void radii, $f(R)$ abundances seem to approach the GR values. Given the considerable error for the void abundance at large $r_{\rm void}$, this may simply be a statistical fluctuation. However, we remark here that such a behaviour might also be physical. Even though the fifth force makes halo formation more efficient in $f(R)$ voids, the density in the largest voids could be so low that not many new haloes form after all, and the relatively small number added to the halo number density still allows these voids to be identified as in GR. This possibility needs to be investigated with care in larger volume simulations, which have better statistics.

For small voids, model differences for the abundances are also smaller. It is possible that small voids are emptier of haloes by definition, since our void finding algorithm ensures that they contain no haloes above our mass threshold within $r_{\rm void}$. The abundance of cosmic web structures within small voids is likely to be lower than in large voids. The fifth force in small voids expels mass out of the

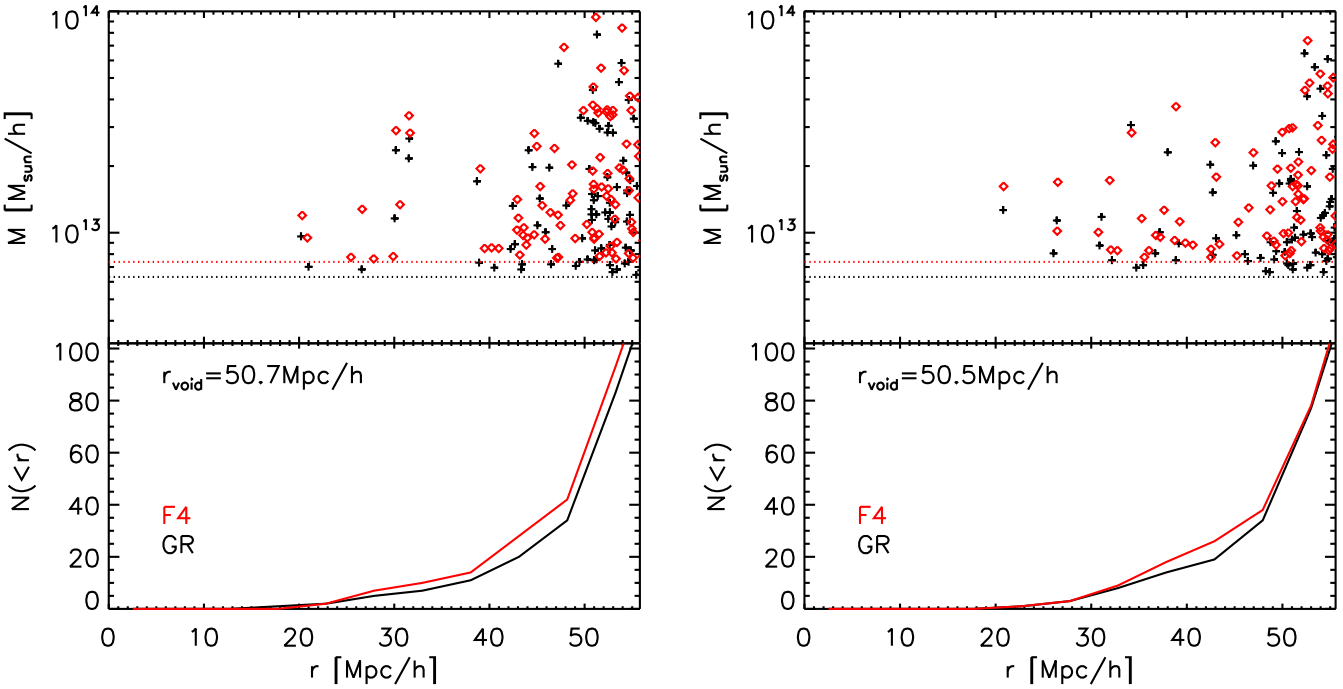


**Figure 7.** The two largest voids found in our GR simulations using haloes above $10^{12.8}\,M_\odot\,h^{-1}$, as indicated by the black-dotted lines. On the top panels, each black cross represents the radial distance of a halo from the void centres versus the halo mass. The red diamonds are the haloes found within the same comoving radius from the same GR void centres, but from the simulation for the F4 model; the halo mass cut for this model is indicated by the red dotted line. The slight differences between the black dotted and red dotted lines are to make sure that the number density of haloes between these two models are the same. Bottom panels show the cumulative number of haloes from the centre of the GR voids. The F4 curves being above the GR curve suggests that more haloes form within these void regions in F4 than in GR.

void region, but fails to trigger much more halo formation, simply because there are not many structures in it for new haloes to form.

Quantitatively, by adopting as error the scatter of the abundance from 1 Gpc $h^{-1}$ sub-volumes of the 1500 Mpc $h^{-1}$ simulations, we can estimate the signal-to-noise (S/N) ratio of the fractional difference between $f(R)$ models and GR (the scatter is shown as shaded areas in Fig. 5). The S/N peaks at approximated 30 Mpc $h^{-1} < r_{\rm void} < 40$ Mpc $h^{-1}$, where void abundance in F4, F5 and F6 is lower than in GR with a S/N = 14, 6 and ∼2 at their peak, respectively, as shown in Fig. 6. The significance of the difference clearly depends on the adopted value for the minimum void size. In principle, with a larger volume, as the statistics of large voids increases, the peak of S/N may shift towards larger radius.

In all cases, the samples of voids are well centred as evidenced by the $\sigma_4$ values obtained for the voids. The inset in Fig. 5 shows the distribution of $\sigma_4$ for GR; as can be seen it peaks at $\sigma_4 \simeq 0.05$, indicating an accuracy of better than 5 per cent the void radius in its centre. The histogram of $\sigma_4$ has a long but very low tail extended to larger values. This suggests that the majority of voids identified are perhaps close to spherical. Only a small subset of voids has a large value of $\sigma_4$, which are perhaps very different from spherical or are fake voids. With the $\sigma_4$ value for each void, we can control the quality of our void sample. We will later use cuts in this parameter to select sub-samples of improved statistical value.

In summary, dark matter void abundances are greater in $f(R)$ than that in GR. In contrast, halo voids show the opposite trend, that relatively large voids are less abundant in $f(R)$ gravity than in GR, and their differences are much smaller than in the case of dark matter voids. This rings an alarm that voids identified from tracers are very different from those from dark matter. We will see this further on in terms of void profiles. Moreover, the decrease of halo void abundances in $f(R)$ model may also provide a unique observable to break parameter degeneracies between $f_{R0}$ and $\sigma_8$ in the ΛCDM model. In ΛCDM, the abundance of large voids is expected to increase with the increase of $\sigma_8$. For the same initial conditions, $f(R)$ gravity also shows enhancement of power over a ΛCDM model at late times, which mimics an increase of $\sigma_8$ (though the shape of power spectrum in $f(R)$ model is more complicated than a simple increase of amplitudes over a ΛCDM model, see (Li et al. 2013) for more details). So, if one observes an effective $\sigma_8$ that is greater than expected from the concordance ΛCDM model, it is not easy to tell whether the Universe is just ΛCDM with a higher $\sigma_8$, or if it is $f(R)$. With the halo void abundance in $f(R)$ model being smaller than that in GR, we expect that this degeneracy can be broken.

### 4.3 Void-in-cloud frequency

The effect of the fifth force in $f(R)$ gravity makes voids emptier, but this in turn could result in changes in the frequency of voids that form within overdensities, i.e. of void-in-cloud voids (Sheth & van de Weygaert 2004). With our adopted criterion to separate void-in-clouds we measure their fraction as a function of void radius, and show the result in Fig. 8.

The left-hand panel shows the results for voids identified using the dark matter particles, and the right-hand panel corresponds to when using dark matter haloes as tracers of the density field. As can be seen, the fraction of void-in-clouds in the dark matter density field increases from GR through F6 and F5 to F4. For the latter, this fraction is ∼30 per cent higher than for GR, almost constant with

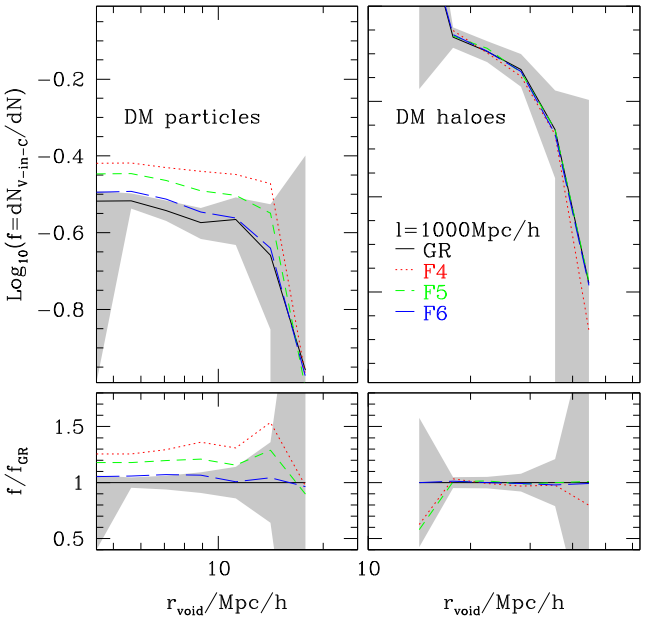


**Figure 8.** Fraction of void-in-cloud voids as a function of void radius, for the GR, F6, F5 and F4 models (different line types as shown in the key). The bottom panel shows the ratio of the fractions with respect to GR.

void radius. The differences are smaller, of only ∼5 per cent for F6, making this a difficult test on its own to separate $f(R)$ gravity from GR, but that can provide further constraining power when used in conjunction with abundances, and also with void profiles, a subject we will turn to in the next section.

When using dark matter haloes to identify voids (right-hand panel), the fraction of void-in-clouds is substantially higher than for voids identified using dark matter particles. However, the differences between the $f(R)$ models and GR almost disappear.

The fact that $f(R)$ gravity produces more void-in-clouds reflects the fact that in $f(R)$ gravity, underdense fluctuations in the overdense environments are more likely to develop into voids that are selected by our algorithm, because the repulsive fifth force is stronger for void-in-clouds (Clampitt et al. 2013): the consequence of this is more voids are generated in overdense regions. Note that the higher void-in-cloud frequency is mainly true for dark matter voids, but not obvious for halo voids: this is probably due to the sparse sampling of haloes.

## 5 VOID PROFILES

We have seen from the above section that void abundance can be a powerful probe of $f(R)$ gravity when using haloes to identify voids. In this section, we shall study the other basic property of voids, their profiles, and see whether stronger constraints can be obtained here. We will look at both the density and velocity profiles of voids.

From this point on we will only use voids identified in the halo fields for two reasons. The first is to mimic observational data that consists of galaxies. The second is related to the findings from the previous section: as results using haloes as tracers produce smaller differences between $f(R)$ gravity and GR, this choice will provide the minimum possible difference that would need to be detected to tell apart these different models.

We start from the halo void catalogue that allows 0–50 per cent overlapping with neighbouring voids. The 50 per cent is the ratio of the distance of two void centres versus the sum of their radii. For some extreme cases where one void is much smaller than the other, the small ones can still be a sub-void of the larger one, and they both pass our selection criteria. To avoid this, by default, we also exclude sub-voids that are 100 per cent contained by a larger voids. We also exclude voids with shape parameter $\sigma_4 > 0.2$ to make sure that most of them are close to spherical. In general, changing these criteria does not affect most of our results qualitatively, but quantitatively, it may. We will address this in more detail in Section 5.2.

### 5.1 Void density profiles

#### *5.1.1 Halo number density profiles of voids*

We first investigate whether there is any difference for the dark matter halo distribution around voids. This has direct observational implications as one can simply use the observed tracers (galaxies and galaxy clusters) for this measurement (P05).

With void centres and radii found from halo fields, we count the number of haloes in spherical shells of the thickness of $0.1r_{\rm void}$ from a given void centre and divide them by the comoving volume of each shell to obtain the halo number density profiles of voids. We rescale each halo-to-void-centre distance by the void radius before stacking them. Results are shown in Fig. 9, where error bars show the scatter about the mean for the void samples obtained from our 1 $(\mathrm{Gpc}\,h^{-1})^3$ volume within the radius ranges shown in the legend. Error bars are plotted only for the GR lines for simplicity; the sizes of error bars are similar for the other models, as we have checked explicitly. The radius ranges of 15–25 Mpc $h^{-1}$ and 35–55 Mpc $h^{-1}$ are chosen to represent approximately the two different types of voids, void-in-cloud and void-in-void (see Sheth & van de Weygaert 2004; Cai et al. 2013; Ceccarelli et al. 2013; Hamaus et al. 2014).

We find that all profiles have very sharp rising features at $r_{\rm void}$. For small voids (left-hand panel), there are striking overdense ridges at $\sim r_{\rm void}$, and the profiles decrease gradually with $r$ to reach the mean number density at $r \sim 2.5r_{\rm void}$. For large voids (right-hand panel), there is no clear overdense ridge, and the profiles increase asymptotically towards the mean density, before reaching it at $r \sim 1.5r_{\rm void}$. The profiles of the small and large voids are qualitatively as expected for void-in-clouds and void-in-voids (Cai et al. 2013; Ceccarelli et al. 2013; Hamaus et al. 2014), though there is no clear division in void size for these two types, as we have checked explicitly. In general, smaller voids have steeper profiles than larger ones, with more prominent overdense ridges. For the very small voids in our catalogues, their overdense ridges are so prominent that they overcompensate the halo number (or mass) deficit within $r_{\rm void}$. This reflects itself as the inflow of mass towards the void centre beyond a certain radius, as will be shown in Section 5.3.

It seems that the halo number density profiles of GR and $f(R)$ gravity are extremely close to each other. This is not surprising for the following reason. Our void finding algorithm requires the number density of haloes to satisfy the same density criteria of 0.2 times the mean, and we do not expect to find strong differences of void profiles at least within $r_{\rm void}$, as shown in the bottom panels of Fig. 9.

In general, each dark matter halo does not necessarily correspond to one galaxy. If one uses galaxies as tracers to find voids and measures the resulted galaxy number density profiles of voids, the number of galaxies occupied in each halo will put different weights to haloes with different masses. This could make the void profiles look different from those presented in Fig. 9. However, as shown by P05, the use of galaxies instead of dark matter haloes has a

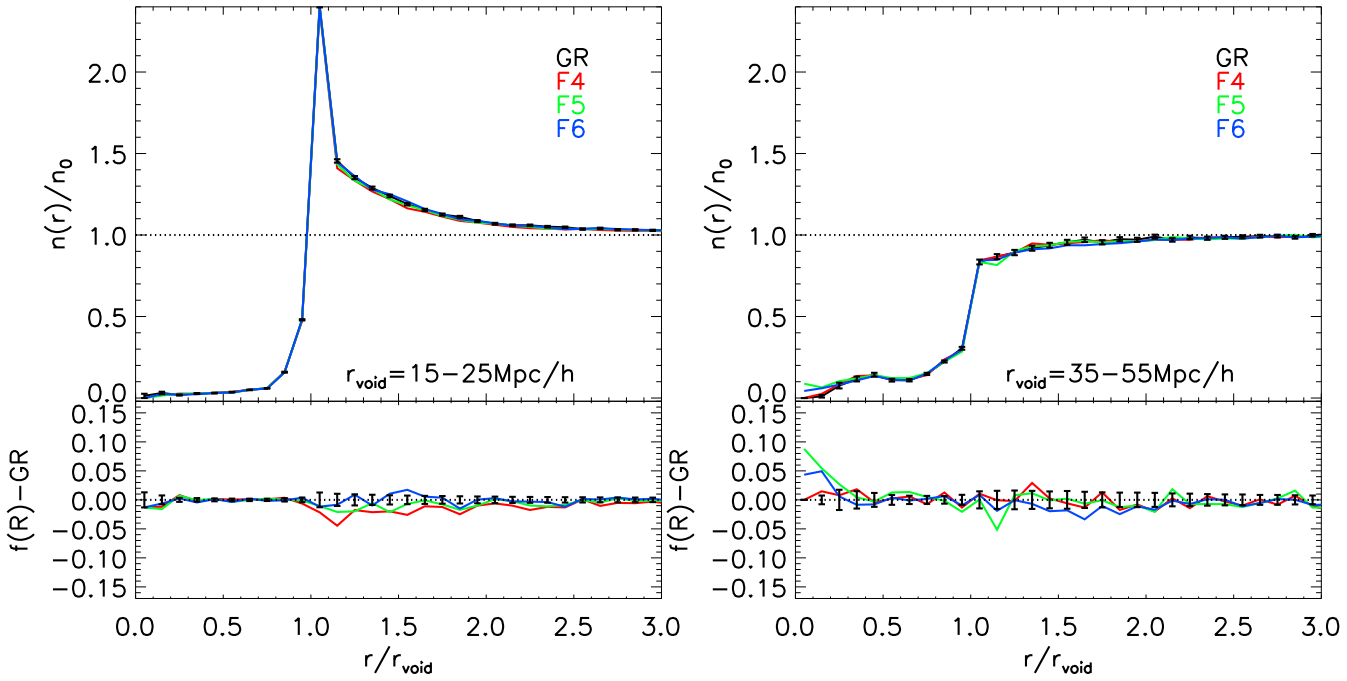


**Figure 9.** Top panels: void density profiles measured using haloes above the minimum halo mass of $M_{\rm min} \sim 10^{12.8}\,{\rm M}_{\odot}\,h^{-1}$ from simulations of different models as labelled in the legend. $M_{\rm min}$ is slightly different from $10^{12.8}\,{\rm M}_{\odot}\,h^{-1}$ in the $f(R)$ models so that the number of haloes for different models are the same (see the text for more details). Error bars shown on the black line (GR) are the scatter about the mean for voids at $15\,{\rm Mpc}\,h^{-1} < r_{\rm void} < 25\,{\rm Mpc}\,h^{-1}$ (left) and at $35\,{\rm Mpc}\,h^{-1} < r_{\rm void} < 55\,{\rm Mpc}\,h^{-1}$ (right) found within the $1({\rm Gpc}\,h^{-1})^3$ volume. There are [6038, 5946, 6096, 6307] (left) and [296, 323, 319, 261] (right) voids in GR, F6, F5 and F4 models passing the selection criteria. Bottom panels: the absolute differences obtained by subtracting GR predictions from the corresponding $f(R)$ values (note that we do not show the relative difference here because the void density profile can be close to zero near the void centre, making the relative difference noisier and less informative; the same holds true for Figs 10–13).

small impact on the measured void properties. Moreover, assuming that the weights are similar for the different models, the differences between $f(R)$ gravity and GR, which are the main concern of our study, should remain similar. We therefore do not intend to explore beyond using haloes for the present study.

Model differences in void profiles might not be seen if void profiles are self-similar, i.e. if voids in $f(R)$ models grow larger than those in GR without changing their shapes, the rescaled void profiles will look the same. In other words, when looking at voids within the same radius range in different models, one may be comparing different void populations. To check if this happens for the results in Fig. 9, we test using void centres found in the GR simulation to measure the halo number density profiles for $f(R)$ simulations. This makes sure that we are comparing the same void regions of the same initial conditions. Any differences from GR should be purely due to the different structure formation process in $f(R)$. Results are shown in Fig. 10. Interestingly, we find that voids are less empty of haloes in $f(R)$ models than in GR within $r_{\rm void}$. To check if the differences are due to the slight difference in the minimal halo masses among different models, we have also used halo catalogues of the same $M_{\rm min}$ to measure the profiles, and the results shown in Fig. 10 are confirmed.

Naively, the fact that voids in $f(R)$ models are not as empty of haloes as in GR may seem counter intuitive and contradict the conventional picture of voids in chameleon models. For example, the analytical study of Clampitt et al. (2013) suggests that voids should expand faster hence become emptier in these models. However, it is important to recall that voids defined using tracers (haloes) may be very different from the actual dark matter voids. When looking at haloes, as we do here, the above conclusion is understandable and consistent with what has been shown in Fig. 7. Namely, in $f(R)$ models the fifth force is likely to be unscreened in void environments, which makes haloes form earlier and become more massive. Voids therefore become less empty than in GR if they are defined using dark matter haloes of a similar $M_{\rm min}$.

It is also noticeable from Fig. 10 that the overdense ridges at $r \sim r_{\rm void}$ in $f(R)$ models are not as sharp as in the GR case. There are two possible reasons for this. First, since some of these void regions in $f(R)$ models do not correspond to voids in GR, or have slightly different radii from their GR counterparts, including them for the stacking smears the ridge slightly.

Secondly, within the same overdense regions, especially at the overdense ridges, the merger and mass accretion rate of haloes may be higher in $f(R)$ models due to the fifth force, which can actually decrease the number of haloes exceeding a minimum cutoff in those particular regions. If this is true, one may expect the mass contained in our selected $f(R)$ gravity haloes to be no less than that contained in the GR haloes, though the number of haloes can be smaller in the former case (as shown in Fig. 10), due to mass conservation. To test this, we have calculated the void profiles of the mass which is actually contained in haloes. Results are shown in Fig. 11. For better illustration, we have normalized all profiles in these two figures by the density of mass contained in the GR haloes. Comparing Fig. 10 with Fig. 11, it is clear that although the halo number density profiles are lower in $f(R)$ voids, the masses contained in these models are greater than that in GR, confirming that haloes grow more rapidly, by faster accretions and/or mergers, in the former cases.

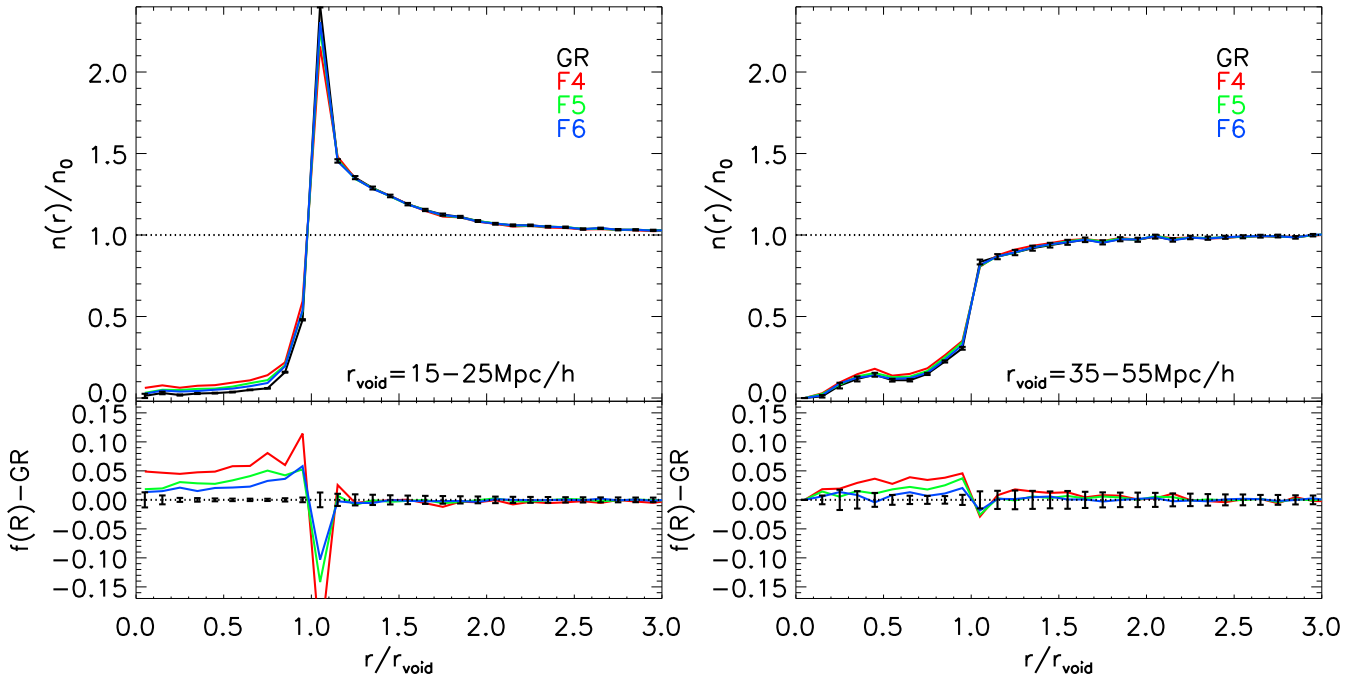


**Figure 10.** Similar to Fig. 9, but showing the halo number density profiles using the void centres from the GR simulation and applying them to measure the profiles for halo catalogues of $f(R)$ models. This is to remove the effect present in Fig. 9 where void populations in different models might be different. Any difference presence in the profiles here should purely due to the action of the fifth force.

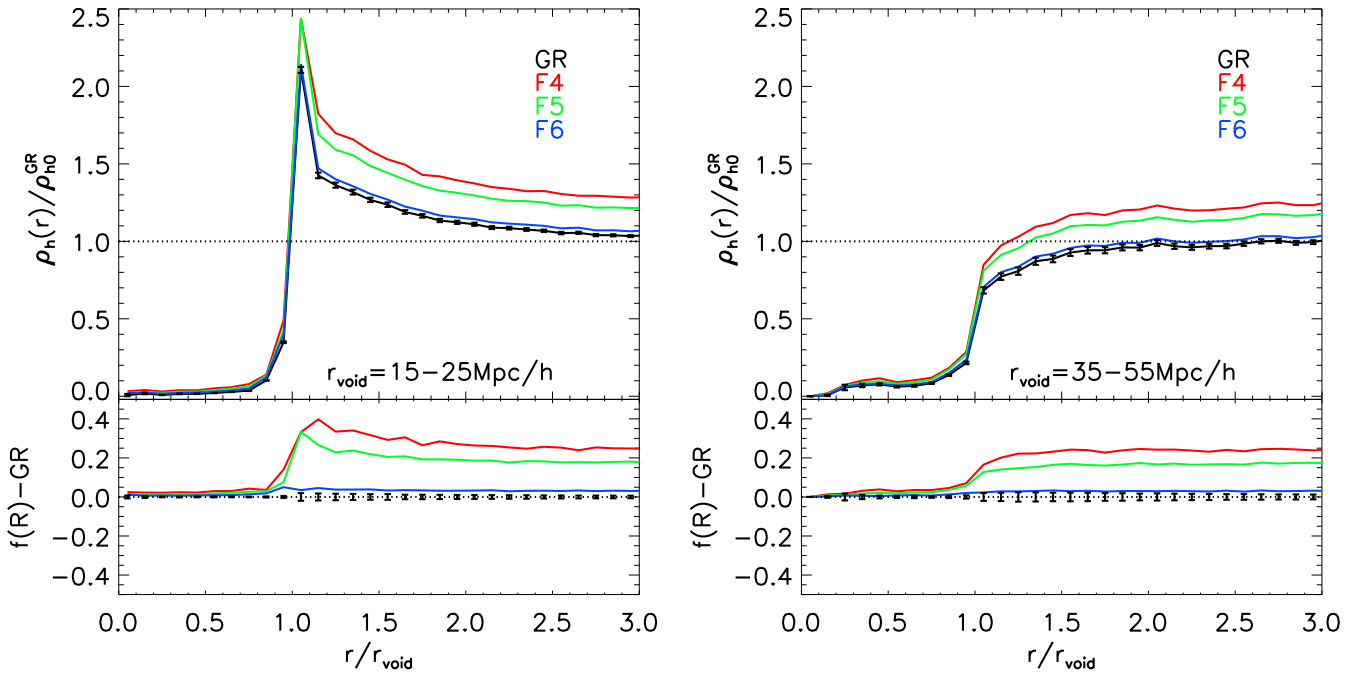


**Figure 11.** The void profiles for the mass contained in haloes. For better illustration, the profiles are normalized by a common denominator, the mass density of haloes above $M_{\rm min}$ in the GR simulation. This plot is used to help understand the counter-intuitive behaviour seen in Fig. 10, and for a direct comparison with the latter, all voids are found using GR void centres (see the main text for more details).

Note that the numerical experiments shown in Figs 10 and 11 are purely for the understanding of the physics in $f(R)$. It is not possible to use voids found in one universe to measure the void profiles of another. What we can observe should be something similar to Fig. 9, i.e. using tracers of a universe to measure the void profiles in the same universe. In this sense, we conclude that in $f(R)$ models, void profiles seen in halo number density are not distinguishable from the GR results. The situation may be different for dark matter profiles of voids. With this in mind, it is important to understand the connection between void profiles of halo number density and those of dark matter, which is to be addressed in the following subsection.

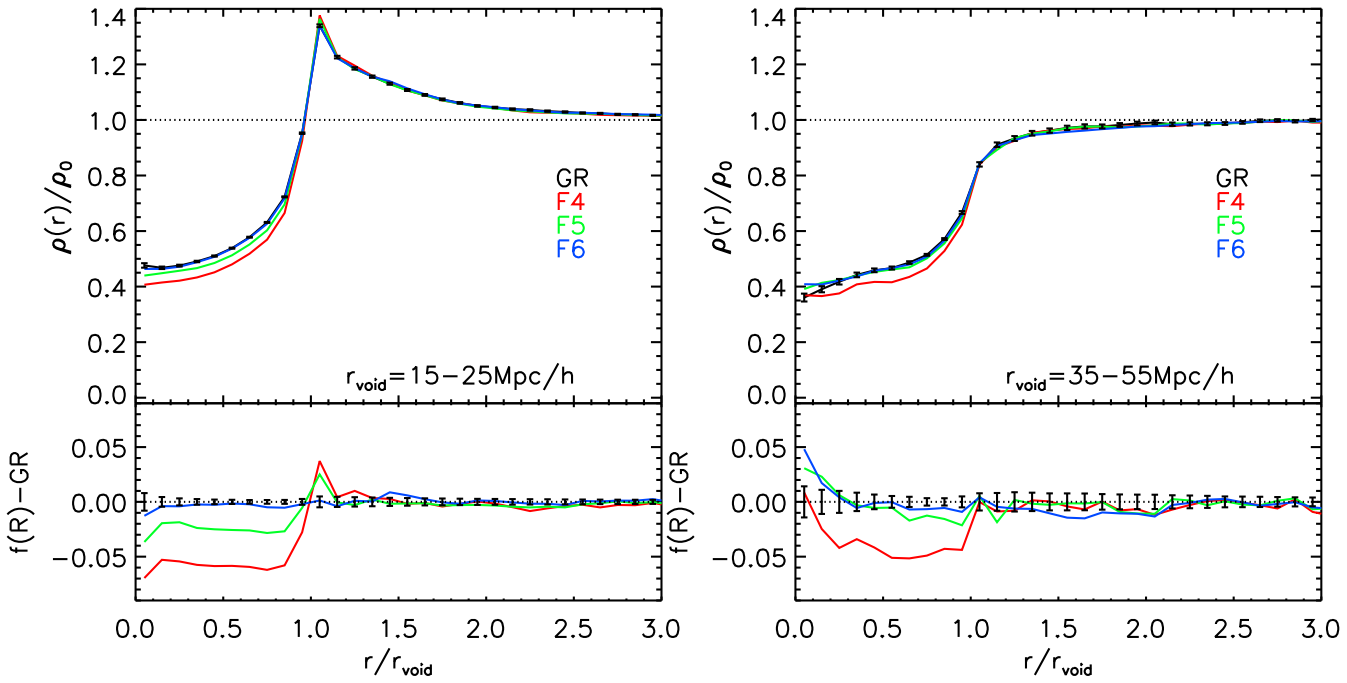


**Figure 12.** Similar to Fig. 9 but showing void density profiles measured using all dark matter particles from simulations of different models as labelled in the legend. Voids are defined using halo number density fields, which are the same as those being used to make Fig. 9.

### *5.1.2 Dark matter density profiles of voids*

With void centres and radii found from halo fields, we measure the dark matter density profile for voids using all dark matter particles, and rescale them in the same manner as for the halo number density profiles. Results are shown in Fig. 12, in which the error bars show the scatter about the mean for the void sample selected from our 1 (Gpc $h^{-1}$)$^3$ volume within the radius ranges indicated in the legend. Again, we only show error bars for the GR lines for clarity.

As we have seen above, relatively small voids are much more likely to live in overdense environments, while big ones are likely to reside in underdense environments. This can be clearly seen in Fig. 12 where small voids (left-hand panel) have an overdense ridge at $\sim r_{\rm void}$, as expected for void-in-clouds, but not for large ones (right-hand panel). These are qualitatively similar to the void halo number density profiles shown in Fig. 9. We have found very smooth density profiles with negligibly small error bars for all cases, which reflects the success of our void-finding algorithm in identifying voids using haloes that are associated with the underlying dark matter distribution.

For relatively small voids (left-hand panel of Fig. 12), the dark matter density profiles have a very steep rising feature at approximately $r_{\rm void}$, and cross the cosmic mean density at about the same place. This is somewhat surprising since the void radius is defined in the halo field by looking for the maximal radius that has $n(< r)/\bar{n} \leq 0.2$. There is no a priori requirement in the definition of what the differential or cumulative density profile of dark matter should be like. This can be understood as that the halo field traces well the dark matter field in void regions.

More interestingly, it is noticeable that $f(R)$ voids are deeper than GR ones at $r < r_{\rm void}$, and F4 is the deepest. At $r > r_{\rm void}$, there is an indication that the overdensity ridges are more prominent in $f(R)$ gravity than in GR. This can be more clearly seen in Fig. 13, where void profiles in different models are measured using void centres found in the GR simulation. Overall, we can conclude that voids in $f(R)$ gravity are emptier (in terms of dark matter) at $r < r_{\rm void}$, even though their halo number densities are the same (cf. Fig. 9) or follow the opposite trend (cf. Fig. 10) in the same regime. Meanwhile, the overdensity ridges may be slightly more prominent in $f(R)$ than in GR.

The behaviour of dark matter density profiles are now in good agreement with our expectation for $f(R)$ model. Theoretical calculations have found that the fifth force in void regions is repulsive in these models, driving the expansion of walls of voids to go faster, and making voids emptier than in GR (Clampitt et al. 2013), which is what we see in Figs 12 and 13.

The situation for relatively large voids (the right-hand panels of Figs 12 and 13) is similar to that of the small ones except that there is no overdense ridge for the void profiles. After rising sharply at $r \sim r_{\rm void}$, the profiles gradually approach to the cosmic mean, before eventually reaching it at $\sim$1.5 $r_{\rm void}$. The differences among different models for large voids are also somewhat smaller, especially when the void profiles in all models are calculated using GR void centres (Fig. 13). This agrees with the analytical calculations of Clampitt et al. (2013) that the model differences in terms of void expansion is greater in void-in-clouds than void-in-voids.

The good agreement between Figs 12 and 13 suggests that the difference we find in Fig. 12 is physical. Nevertheless, the test of Fig. 13 is a thought experiment that does not happen in real observations. If we select voids within a certain range of radii, their stacked profiles would encode the differences of void populations as well as their evolution history. In this sense, the results shown in Fig. 12 have more practical meaning.

In summary, the results of this subsection unveil the complexity of voids in $f(R)$ gravity. There are clear differences between the profiles of voids identified using tracers and those identified using dark matter. This makes it more challenging to use them to place observational constraints. In the next subsection, we will explore the possibility of using weak gravitational lensing of galaxies by

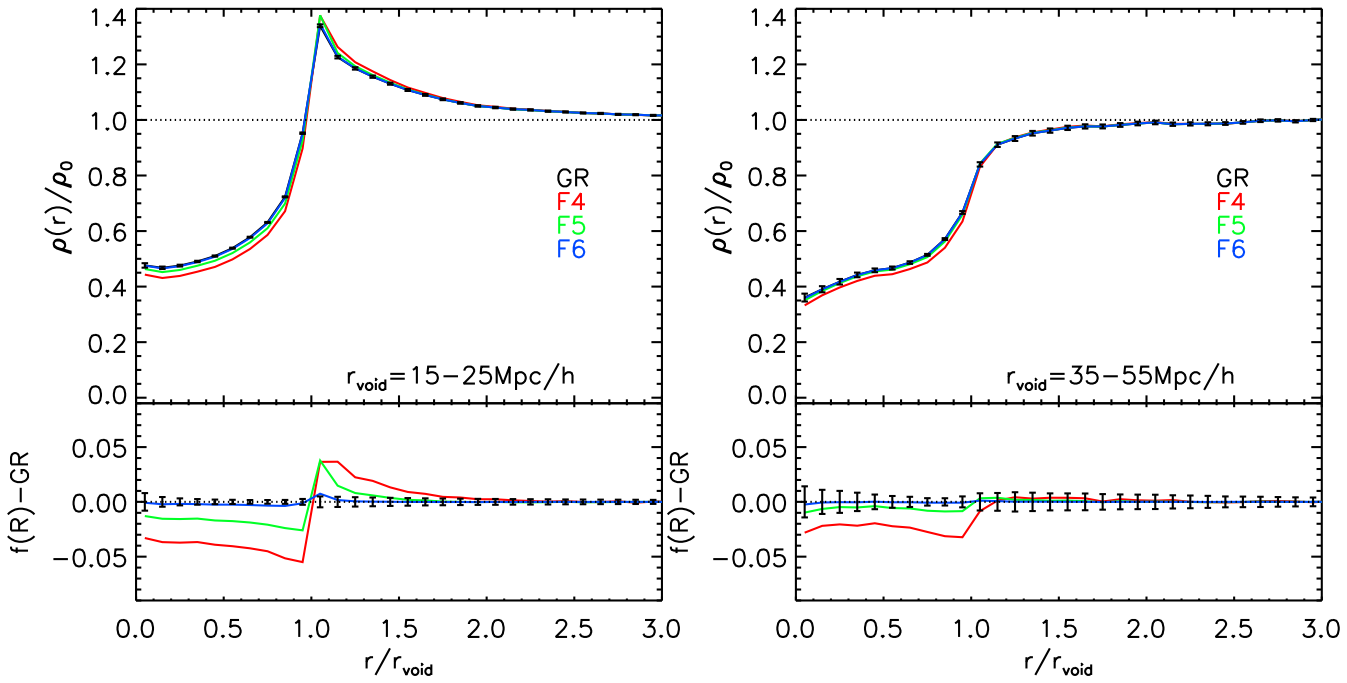


**Figure 13.** Similar to Fig. 12 but showing results using GR void centres to measure void profiles with simulations of different $f(R)$ models. This is to remove the effect present in Fig. 12 where void populations in different models might be different. Any difference presence in the profiles here should purely due to the action of the fifth force.

voids to constrain these models. Although observationally the direct identification of voids can only be done using tracers (haloes in our case), the lensing signal generated by voids are associated with their underlying dark matter distribution. Consequently, the combination of the two may provide perspectives of tighter constraints on $f(R)$ gravity.

### 5.2 Lensing tangential shear profiles

The dark matter profile shown in Fig. 12 can in principle be measured using weak gravitational lensing. Voids defined using tracers (haloes or galaxies) are closely associated with density decrements along the line of sight, as mentioned in Section 5.1. The deflection of light propagating through voids causes distortions to the shapes of background galaxies. The weak lensing shear signal of the background galaxies can be used to measure the matter distribution associated with the foreground voids (Amendola, Frieman & Waga 1999; Higuchi, Oguri & Hamana 2013; Krause et al. 2013). This technique is similar to using galaxy–galaxy lensing to measure the density profile of dark matter haloes. The key quantity that connects observations and theoretical predictions is the tangential shear $\gamma_t$ of the shape of the background galaxies. It is proportional to the excess of projected mass density along the line of sight,

$$\Delta\Sigma(R) = \gamma_t \Sigma_c = \Sigma(<R) - \Sigma(R), \tag{12}$$

where $\Sigma_c$ is the geometric factor defined as

$$\Sigma_c \equiv \frac{c}{4\pi G} \frac{D_A(z_s)}{D_A(z_l) D_A(z_l, z_s)(1+z_l)}. \tag{13}$$

Here, $D_A(z_s)$ and $D_A(z_l)$ are the angular diameter distances from the observer to the source and the lens, respectively, and $D_A(z_l, z_s)$ is the angular diameter distance between the lens and the source. $\Sigma(R)$ and $\Sigma(<R)$ are the projected surface densities around the centre of a void at the projected distance of $R$ and within $R$. They are related to the cross-correlation function of void centres and dark matter via:

$$\Sigma(R) = \bar{\rho} \int [1 + \xi_{vm}(\sigma, \pi)] \mathrm{d}\pi, \tag{14}$$

where $\xi_{vm}(\sigma, \pi)$ is the 2D cross-correlation function of void centres and dark matter. $\sigma$ and $\pi$ are the transverse line of sight and the line-of-sight separations. For simplicity, we drop the $\bar{\rho}$ factor and work on dimensionless quantities. $1+\xi_{vm}(\sigma, \pi)$ is essentially the 2D density profile of voids. To increase the S/N, we do a similar stacking as for the 1D profiles. Each void is rescaled by its radius before stacking. We have bins along the $\sigma$ and $\pi$ directions of width of 0.1 $r_{\rm void}$, and use equation (14) to integrate along the line of sight up to 2 $r_{\rm void}$, where the density comes back very closely to the background (see Fig. 12). Results are shown in Fig. 14. For simplicity, we show the profiles from stacking all voids in our 1 (Gpc $h^{-1}$)$^3$ simulation box. The tangential shear signal peaks at $r \sim r_{\rm void}$ where the 1D matter density profiles are the steepest. This is expected as $\Sigma(<R) - \Sigma(R)$ is sensitive to the slope of the density profile. Close to the centre of the void, or further away from the void, the density profiles are relatively flat, hence the tangential shear signal is small. But the signal can still be significant at a few times the void radius, as shown in the left-hand panel of Fig. 14.

There is little difference between $f(R)$ gravity and GR for the lensing tangential shear profile close to void centres. To distinguish between different models, it is more promising to use the shear signal at $0.7 r_{\rm void} \lesssim r \lesssim 1.7 r_{\rm void}$, where the tangential shear profiles may differ most. Quantitatively, this is illustrated by the cumulative S/N shown on the right-hand panel of Fig. 14. The contribution for the S/N from $r < r_{\rm void}$ is relatively minor. The S/Ns rise sharply at $r = r_{\rm void}$; they peak at about 1.5 $r_{\rm void}$, reaching 4 and 8, respectively for F5 and F4. With the line-of-sight projection, F6 is not distinguishable from GR.

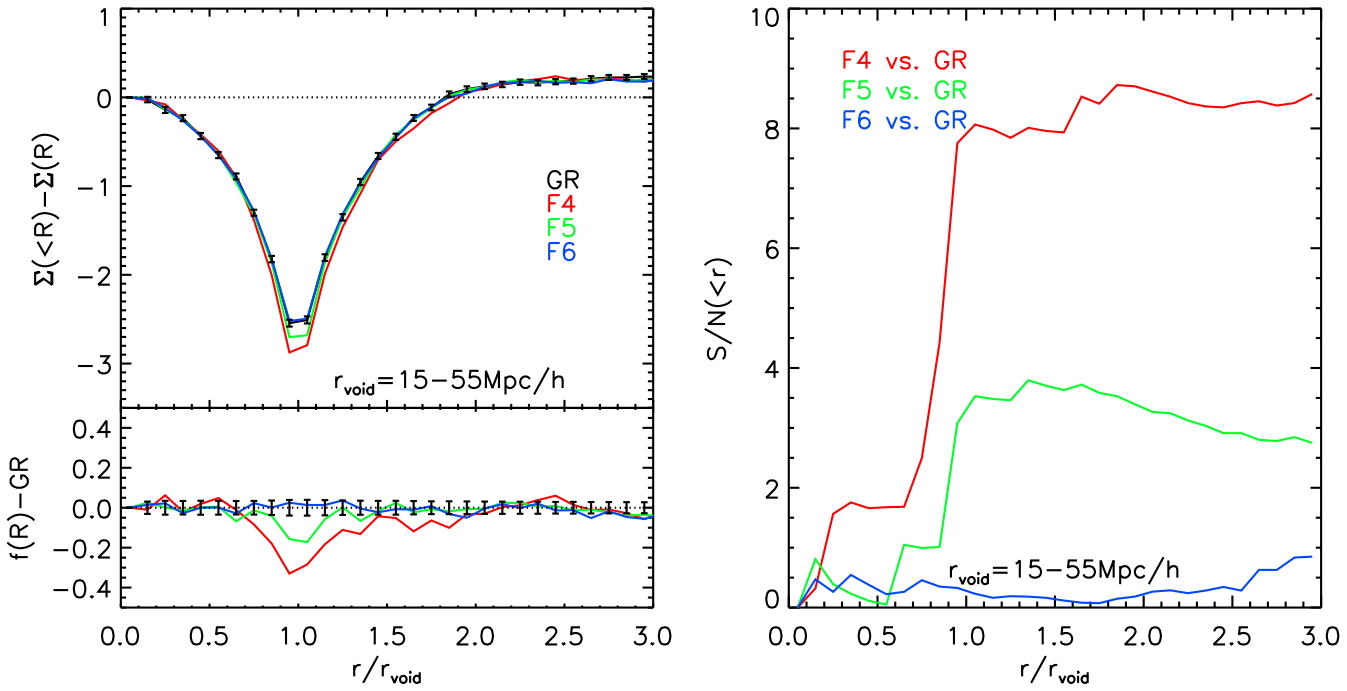


**Figure 14.** Left: like Fig. 12 but showing the lensing tangential shear profiles from stacking all voids with $15 < r < 55$ Mpc $h^{-1}$. They are projected over two times the void radius along the line of sight. $\Sigma(<R) - \Sigma(R)$ is proportional to the surface mass density within the projected radius of $R$ to which we subtract the surface mass density at $R$. Bottom panel: the absolute differences between the black curve with other coloured curves (note that we do not show the relative difference here because the tangential shear can be close to zero near the void centre, making the relative difference noisier and less informative). Right: the corresponding cumulative (from small to large radius) S/N for the differences between GR and $f(R)$ models.

Note that the error bars given are just for the void sample from a volume of 1 (Gpc $h^{-1}$)$^3$. The current Baryon Oscillation Spectroscopic Survey (BOSS) DR11 CMASS sample has an effective volume of 6.0 (Gpc $h^{-1}$)$^3$ (Beutler et al. 2014; Anderson et al. 2014; Sánchez et al. 2014). In principle, the error bars shown in our figures should go down by a factor of 2.4 and the significance level should go up by the same factor if the BOSS DR11 CMASS sample is used, on condition that a deep lensing survey covering the same area of the sky is available. The future *Euclid* survey (Laureijs et al. 2011) is expected to have an effective volume of ∼20 (Gpc $h^{-1}$)$^3$, a factor of 4.4 improvement is expected in this case.

With our simulations, we explore the dependence of S/N for distinguishing $f(R)$ and GR models using the tangential shear signal on various aspects. First, we find that including sub-voids is still useful to help increasing the S/N. With all sub-voids in our catalogue included, the number of voids increases by approximately 76 per cent. This helps to increase the S/N to 7, and 12 for F5 and F4, respectively, but F6 still cannot be told apart from GR, as its S/N does not improve. Secondly, including voids with larger values of $\sigma_4$ (which means including voids that are potentially very different from spherical) also helps to increase the S/N, but very mildly. Finally, the projection of large-scale structure could bring extra noises or even bias the lensing signal associated with voids. To test this, we have integrated out to larger line-of-sight distances for the predicted tangential shear signal. Overall, we did not find the results to be biased when we integrated for more than twice the void radii, but the projection of large-scale structure introduced more noise and slightly larger covariances among the errors of different radial bins, as shown in Fig. 15. This makes it harder to tell apart the different lines for different models, especially for large voids. Increasing the line-of-sight projection from 2 to 6 times of void radii deceases the S/N by about 30 per cent.

The last point adds challenges for accurate measurement of the tangential shear profiles of voids. The density contrasts of voids are not as great as those of haloes. In other words, the amplitude of the shear signal associated with voids is relatively small, making it more vulnerable to noises such as that introduced by line-of-sight projection. This could set the upper bound for the power of constraining $|f_{R0}|$ using the tangential shear signal of voids. We have already seen this from the fact that F6 becomes indistinguishable from GR with the contamination of large-scale structure *in a 1 (Gpc* $\mathrm{h}^{-1}$*)*$^3$ *volume*.

Note that we have not included lensing shape noise for this study, since in general, shape noise may be sub-dominant compared to the noise from line-of-sight projection of large-scale structure for a DETF Stage IV type of deep imaging survey (Albrecht et al. 2006). Especially, the effect of shape noise is even less at relatively large radius of voids (Higuchi et al. 2013; Krause et al. 2013), which is the region of our interest to distinguish GR from $f(R)$ gravity. For a lensing survey covering 5000 deg$^2$ of the sky, with the number density of source galaxies being $n_{\rm gal} = 12\,\mathrm{arcmin}^{-2}$, the rms of the ellipticity distribution of galaxies $\sigma_\epsilon = 0.3$ and a mean redshift of ∼1, the lensing shape noise is clearly sub-dominant for the radius shown in their fig. 2, which is about $0.3 \times r_{\rm void}$ (Krause et al. 2013). For a survey of similar settings, Higuchi et al. (2013) also find that lensing shape noise has little effect at large scales [see tables 4, 5 and fig. 6 of Higuchi et al. (2013) for quantitative comparisons for the lensing S/N with or without shape noise.] Therefore, in the regime of $r > 0.7 r_{\rm void}$ where the shear profiles in $f(R)$ gravity differs from GR, it is relatively safe to ignore shape noise for a deep imaging survey. At the very precise level, the importance of shape noise varies with the specific design of the lensing survey as well as how it is combined with the (spectroscopic redshift) survey necessary to identify voids. For example, a deeper lensing survey with good

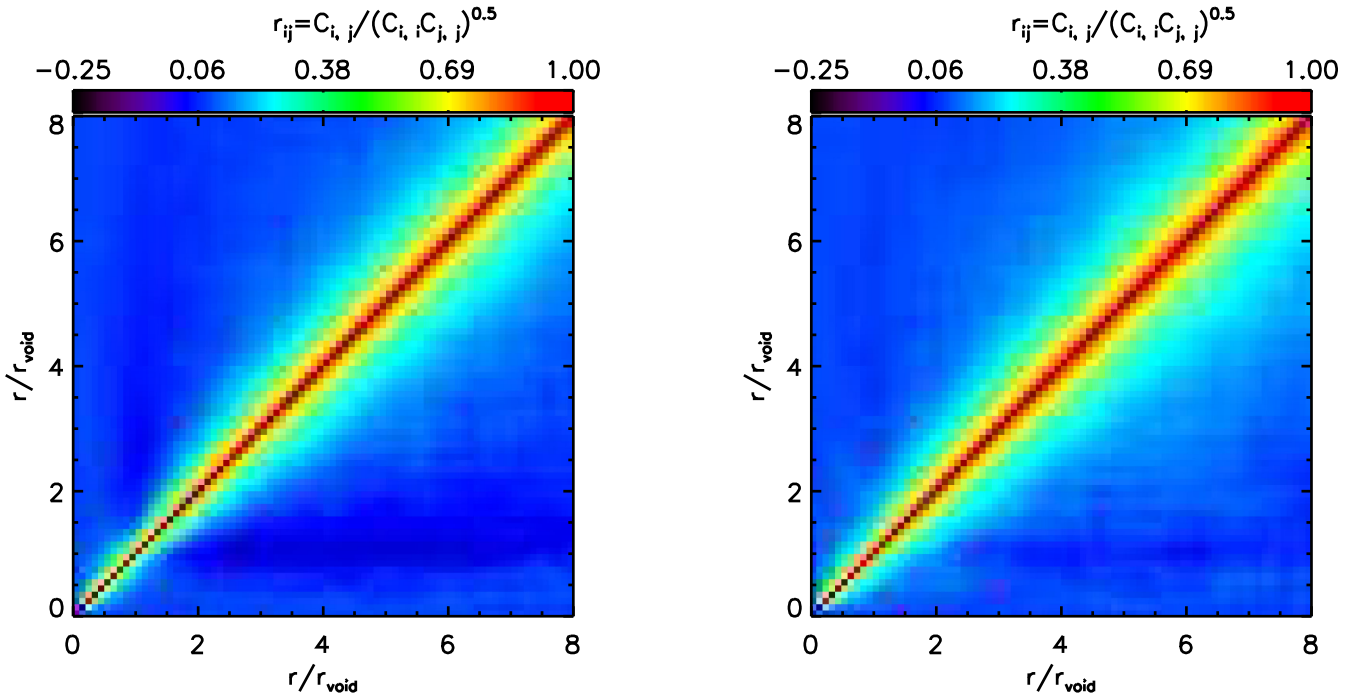


**Figure 15.** Covariance matrices of the predicted lensing tangential shear from stacking all voids with $15 < r < 55$ Mpc $h^{-1}$ from the 1 Gpc $h^{-1}$ a side GR simulation. Left: the projection length along the line of sight is $2\times$ $r_{\rm void}$; Right: the projection length is $8\times$ $r_{\rm void}$.

image quality tends to have smaller shape noise per galaxy, hence the contribution to the noise covariance from lensing shape noise may be relatively minor. We leave it for future studies to figure out the contribution of shape noise for particular surveys.

The first measurements of the lensing shear signal behind cosmic voids has been conducted using the SDSS data (Clampitt & Jain 2014). In their analysis, voids are found using LRGs. The tangential shear signals are measured for the stacked lensing source galaxies behind the stacked void centre. A $13\sigma$ shear signal associated with the stacking of those voids has been found, which seems surprisingly better than expected from Krause et al. (2013).

As a final note, it is possible to combine together the S/N from the lensing shear profiles with the one obtained from a comparison of the abundances of voids found using dark matter haloes (Figs 6 and 14). Assuming no correlations between the measurement of the lensing profiles and the abundances, the S/N between $f(R)$ and GR increases to 18, 11 and ∼2 for F4, F5 and F6, respectively, for a reasonable choice of lower limit in void radius for the abundances, and selection of voids for the shear profiles. Again, this estimate is valid for a 1( Gpc $h^{-1}$)$^3$ volume.

### 5.3 Void velocity profiles

Velocities of dark matter, as the first integral of forces, should in principle react more sensitively to the differences among different gravity models than the density field. To investigate this, we present different components of velocity profiles for dark matter in Fig. 16 and for haloes in Fig. 17.

The radial velocity profiles, shown as solid curves, peak at $r \sim r_{\rm void}$, consistent with the sharp rise in the density profiles. The sign of the radial velocity being positive means there is coherent outflow of mass. For relatively small voids ($r_{\rm void} = 15$–$25$ Mpc $h^{-1}$), the outflow is about 5, 15 and 35 km s$^{-1}$ or ∼5, 15 and 35 per cent greater than GR for F6, F5 and F4 at $r \sim r_{\rm void}$. Results for larger voids ($r_{\rm void} = 35$–$55$ Mpc $h^{-1}$) are shown on the right: they are qualitatively similar to those of smaller voids, except that the matter outflows are much stronger. They peak at $r \sim r_{\rm void}$ at about 300 km s$^{-1}$ for GR, and for F4 it can be greater by nearly 60 km s$^{-1}$. Indeed, this level of difference is mildly greater than that in the density profiles shown in Fig. 12. The fact that the outflow velocity in $f(R)$ gravity is greater than in GR is also expected from the analytical work of Clampitt et al. (2013): in $f(R)$ gravity, the outward pointing fifth force from void centres drives dark matter to evacuate faster from the voids.

At $r > r_{\rm void}$, the radial velocity profiles decrease. For small voids shown on the left, they turn negative at $r \sim 1.5 r_{\rm void}$, which means there is net inflow of mass. This is a clear signature of void-in-cloud configurations. For large voids shown in the right-hand panel, the radial velocity profiles stay above zero, as expected for void-in-void, and the outflow of mass remains beyond $r \sim 3 r_{\rm void}$.

Fig. 16 also presents the mean tangential velocity as well as the radial and tangential velocity dispersions. It is interesting to see that all these components of velocities have similar levels of differences between $f(R)$ models and GR. Fig. 17 presents the same results for haloes. All the above results regarding velocities in the dark matter field are confirmed using haloes, although the latter is noisier. We have also computed the velocity profiles for voids identified using GR void centres. There is very little difference from Fig. 16, where the $f(R)$ and GR void centres are independent.

The velocity dispersion in $f(R)$ models being greater than in GR provides another observable for testing $f(R)$ gravity. Stacking of galaxies around central galaxies in phase space has been proposed to measure the halo mass at a few times the virial radius, and has been applied by Lam et al. (2012) for testing gravity. The level of differences we have found for the velocity dispersion between $f(R)$ gravity and GR are ∼5, 10 and 20 per cent for F6, F5 and F4. These are consistent with what was found in Lam et al. (2012) for the case of stacked haloes in phase space for the same models (see

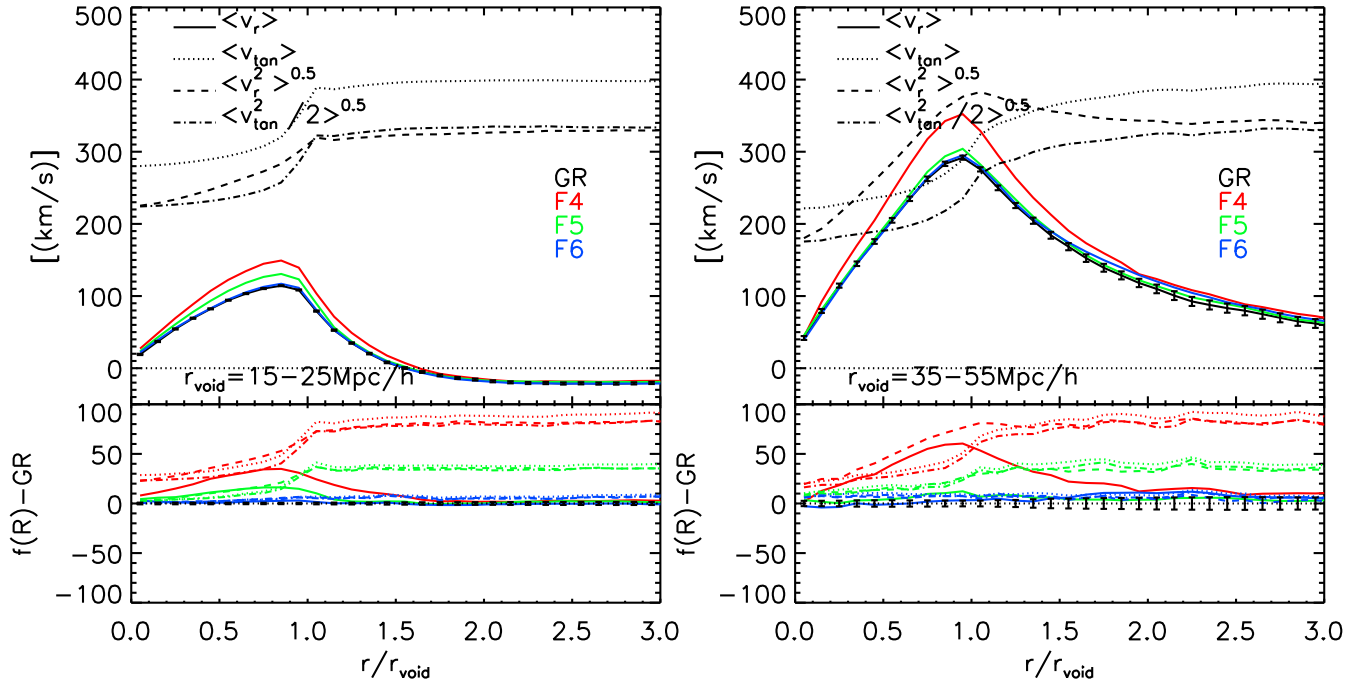


**Figure 16.** Top panels: different components of dark matter particle velocities with respect to the centre of voids defined using haloes for simulations of different models labelled in different colours in the legend. Solid lines – the mean radial velocity profiles; dotted lines – the mean tangential velocity profile; dashed lines – the dispersion of the radial velocities; dash–dotted lines – the dispersion of half of the tangential velocities. For simplicity, for velocity profiles of $f(R)$ models only the radial velocity profiles are plotted. One can appreciate their differences with respect to GR in the bottom panels. Error bars shown on the black line (GR) are the scatter about the mean for voids of $15\,\mathrm{Mpc}\,h^{-1} < r_{\rm void} < 25\,\mathrm{Mpc}\,h^{-1}$ (left) and $35\,\mathrm{Mpc}\,h^{-1} < r_{\rm void} < 55\,\mathrm{Mpc}\,h^{-1}$ (right) found within the 1 $(\mathrm{Gpc}\,h^{-1})^3$ volume. Bottom panels: the absolute differences between the black curve with other coloured curves (note that we do not show the relative difference here because some velocity components can be cross zero at certain radii, making the relative difference noisier and less informative. The same holds for Fig. 17 below).

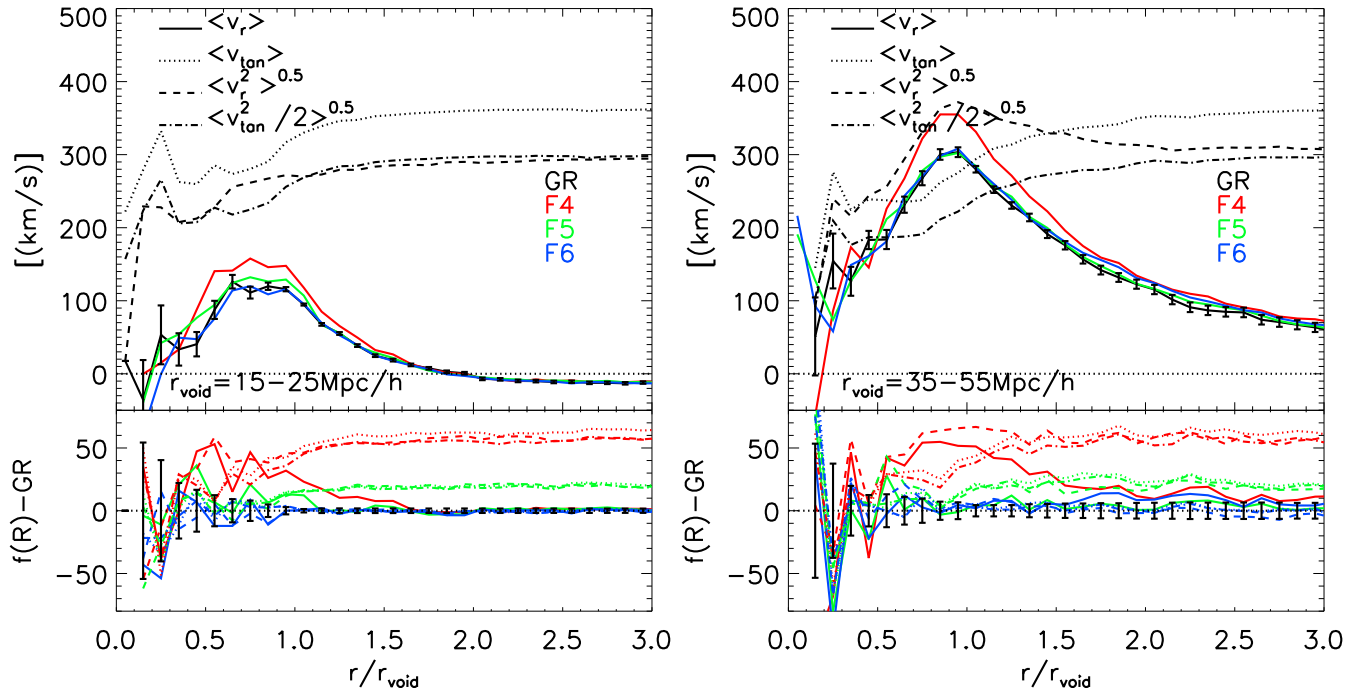


**Figure 17.** Similar to Fig. 16 but showing different components of velocity profiles traced by haloes.

Arnold, Puchwein & Springel 2014; Hellwing et al. 2014, for a test of modified gravity along the same line).

Before leaving this section, we make the following remarks.

(i) The differences in velocity profiles are still present when using haloes as tracers, in contrast to the results from the two previous subsections, supporting the use of tracers to distinguish $f(R)$ gravity from GR. However, model differences in the tangential velocity or radial velocity dispersion are slightly smaller for haloes than for dark matter – which could be a result of the suppression of the fifth force inside haloes – indicating the existence of halo velocity bias in $f(R)$ gravity.

(ii) Differences between models in the velocity and density field can be best captured by the the clustering of voids in redshift space. We will conduct detailed studies of voids in redshift space in a separate paper.

## 6 CONCLUSION AND DISCUSSION

To briefly summarize, in this paper we have studied void properties in $f(R)$ gravity using $N$-body simulations of $f(R)$ (Hu & Sawicki 2007) and GR ΛCDM models of the same initial conditions and the same expansion history. In $f(R)$ models, the repulsive fifth force in voids drives them to grow larger and expand faster. This leads to a range of observables that are potentially powerful to distinguish $f(R)$ gravity from GR. In particular, we have found that:

(i) The void abundances in $f(R)$ gravity can differ significantly from in GR, if voids are identified using the dark matter field. More explicitly, the Hu–Sawicki $f(R)$ model with $f_{R0} = -10^{-4}$ (F4) shows an ∼100–400 per cent enhancement of the void abundance over GR in the void radius range of $10 \sim 20$ Mpc $h^{-1}$; the enhancement in $f(R)$ models with $f_{R0} = -10^{-5}$ (F5) and $f_{R0} = -10^{-6}$ (F6) is smaller, but still at ∼70–100 per cent and ∼20 per cent, respectively, in the same radius range. However, if we (more realistically) identify voids using the dark matter haloes with the same space density, the difference from GR becomes much smaller, nearly disappearing at $r_{\rm void} \lesssim 25$ Mpc $h^{-1}$, for all three variants of $f(R)$ gravity. By using the expected scatter of void abundances, we find that $f(R)$ gravity can in principle be told apart from GR with an S/N=14, 6 and ∼2 for F4, F5 and F6, respectively. Although, in real observations, these may be degraded by the uncertainty of halo mass estimation and the complexity of survey window functions.

(ii) We find the counter-intuitive result that, if voids are identified in the halo field, then $f(R)$ gravity produces fewer large voids ($r_{\rm void} \geq 30$ Mpc $h^{-1}$) than in GR. This is because, thanks to the fifth force, haloes are more likely to form in underdense regions in the $f(R)$ model, which makes low-density regions in this model less empty of haloes even though they are emptier of dark matter. For the same void regions, they are indeed emptier in terms of total dark matter. This suggests that $f(R)$ gravity (or other modified gravities of the similar type) may not be able to resolve the Local Void problem. There are observations suggesting that the Local Void (within the radius of 1–8 Mpc from the centre of the Local Group) seems too empty of galaxies, which may be a problem for the ΛCDM model (e.g. Peebles 2001; Tikhonov & Klypin 2009; Peebles & Nusser 2010), but see (Tinker & Conroy 2009; Xie, Gao & Guo 2014) for different views. There are speculations that a different model with more rapid emptying of voids and piling up of matter on its outskirts may help to resolve the tension (Peebles & Nusser 2010). At face value, it seems that $f(R)$ model is one of such models that has the required feature, as we have seen that the dark matter profiles in $f(R)$ are emptier and the void ridges are sharper. However, the more rapid halo formation in void regions in $f(R)$ models will perhaps make voids less empty of haloes, which is just the opposite to what is needed to resolve the tension. More detailed studies with simulations of better mass resolutions which are able to resolve lower mass haloes are needed to confirm this.

(iii) We find that the halo number density profiles of voids in $f(R)$ gravity are not distinguishable from those of GR. However, the dark matter density profiles associated with these voids are emptier of dark matter in $f(R)$ models than in GR; their overdensity ridges, if any, are more prominent than those in GR. The latter result agrees with previous results based on the spherical expansion model of voids (Clampitt et al. 2013), which predicts that voids in $f(R)$ gravity are emptier and larger. Our results ring the alarm that void profiles can be very different depending on whether we are considering halo number or dark matter density profiles, even just in GR. This is not surprising from our perspective. Haloes or galaxies are biased tracers of the underlying dark matter density field. With relatively massive haloes whose linear bias is greater than unity, we do see the profiles of voids measured using haloes to be steeper than those of dark matter. This is essentially due to the fact that the amplitudes of the large-scale clustering of haloes are greater than those of dark matter. Note that this is different from the conclusion in (Sutter et al. 2014b) that identical radial density profiles between galaxies and dark matter are recovered, though they have used a different void finder, i.e. ZOBOV (Neyrinck et al. 2005).

(iv) Two different types of voids, void-in-cloud and void-in-void are clearly seen in either halo number density profiles or dark matter profiles, the former having sharp overdense ridges but not for the latter. This is consistent with the radial velocity profiles, which indicates a regime of mass inflow for void-in-clouds, but not for void-in-voids. This is also consistent with what has been found using ZOBOV for dark matter from simulations (Hamaus et al. 2014; Paz et al. 2013). For this reason, we argue that in principle it is not possible to find a universal void profile with a single rescaling parameter, i.e. the void radius. A second parameter to characterize the height of the overdense ridge is necessary. Note that this is different from Nadathur et al. (2015) who find that voids in their simulated LRG catalogues are self-similar, but they have used ZOBOV as their void finder for mock and real LRGs, and applied further selections on their voids. Also, it should be noticed that the sizes of voids studied by Nadathur et al. (2015) are on the large size end of the void size spectrum. These are usually of the void-in-void type according to our results and can indeed be described by a radius scaling alone. We find that only smaller voids show a ridge and can be described as void-in-clouds. For them to be described by a density profile formula an extra parameter is needed (e.g. Paz et al. 2013).

(v) We understand the sharp feature in the void-in-cloud case, especially for the halo void profiles, as the nature of large-scale structure and a natural outcome of our spherical void finding algorithm. Haloes are biased tracers of large-scale structure. They live on the skeletons of cosmic web, from which voids are defined. The cosmic web with only massive haloes naturally have vast volume that is empty of haloes. We define our voids by growing maximal spheres that satisfy our number density criteria. Naturally, before the sphere reaches its maximal, it is likely to be completely empty. Once the sphere encounters a halo, it is also very likely to encounter more haloes in the surrounding area, because these haloes are unlikely to be alone, but rather form together in walls and filaments. Meanwhile, we require that the dispersion for the distances from the void centre for the nearest four haloes should be smaller than 0.2 (see the definition of $\sigma_4$ equation 11) (four particles are needed to

have a sphere well defined). This means that there are at least four haloes at the edge of each void. Compared to the volume within the sphere where the number of haloes are nearly zero, this is a large contrast, hence a sharp transition of the profile is expected. Similar features are found by other groups using a similar void finding algorithm (e.g. Pan et al. 2012). They are also qualitatively similar to the results from spherical evolution model (Sheth & van de Weygaert 2004).

(vi) The dark matter density profiles of voids can be measured using weak gravitational lensing. Observationally, this requires the combination of a galaxy redshift survey and a weak lensing (photometric redshift) survey over the same area of the sky. The idea of overlapping sky surveys has been promoted by the combination of redshift space distortion with lensing, which is another powerful way of constraining the linear growth and hence gravity (McDonald & Seljak 2009; Bernstein & Cai 2011; Cai & Bernstein 2012; Gaztañaga et al. 2012; de Putter, Doré & Takada 2013; Kirk et al. 2013). With this setting of surveys, voids will be identified using tracers like galaxies/haloes from the redshift survey. The shear signal of the background galaxies (from the deeper lensing survey) associated with the voids will be stacked around the void centres. We demonstrate that the lensing tangential shear profiles can be used to constrain $f(R)$ gravity. For a survey volume of about 1 $(\mathrm{Gpc}\,h^{-1})^3$, GR can be distinguished from F5 and F4 by $7\sigma$ and $12\sigma$, respectively, when including sub-voids. Most of the signal comes from the edge of the voids where the density profiles are the steepest. The S/N is lower for larger voids as their abundance is much smaller and profiles less steep. We stress that the estimates of S/N are somewhat optimistic since we do not account for lensing shape noise and other systematics. Note that the S/N can be improved by a few times by employing the current BOSS survey or future *Euclid* survey. We also found that including sub-voids is useful for increasing the S/N. Line-of-sight projection of large-scale structure degrades the S/N among models and may set limits on the constraint of $|f_{R0}|$. We find that F6 is not distinguishable from GR in terms of lensing of voids for this reason. These S/N values increase when combining this statistics with the abundances of halo defined voids, making it possible to increase the significance of the difference between F6 and GR to an $\mathrm{S/N} \sim 2$.

(vii) Admittedly, the steepening of dark matter void profiles in $f(R)$ model over GR may have some level of degeneracy with the increase of $\sigma_8$ in $\Lambda$CDM model. This can be checked with GR simulations of different $\sigma_8$. However, the halo void abundance in $f(R)$ being smaller than in GR is a unique feature that might be powerful to break this degeneracy. In this sense, it is important to combine measurements of void abundances and profiles.

(viii) Model differences in the velocity profiles are slightly greater than in the density profiles, and these appear to be as strong when using the mass or tracers to measure velocities. This offers a good opportunity to constrain $f(R)$ gravity by studying voids in redshift space. This is particularly true for F4, which shows the strongest deviation from GR, while the constraints on F5 and F6 will be relatively weaker. A detailed study will be presented in a forthcoming paper.

We caution that our study of void properties are based on using haloes as tracers. In principle, haloes are accessible through the observations of galaxy clusters and groups. Compared with galaxies, this observable suffers from the sparseness of samples and the relatively large uncertainties in determining the halo mass. Therefore, it may seem that galaxies are more direct observables to probe voids. However, the complexity of galaxy formation physics, which is likely to be different in $f(R)$ gravity from GR in a non-trivial manner, will make the definition of voids in different models even more complicated and the results less reliable. In contrast, haloes can be found observationally in different ways, such as using lensing, X-ray clusters and Sunyaev–Zel'dovich effects, which are less affected by the galaxy formation physics. Furthermore, most of our results concern only the number density of haloes rather than their masses, and so are less affected by the uncertainties caused by halo mass measurements (which can be worse in $f(R)$ gravity because haloes can have different dynamical and lensing masses, depending on their masses and environments).

Recently, there has been rapidly growing interest in using cosmic voids to study cosmology or constrain gravity and dark energy models. In the two most well-studied categories of alternative gravity theories, the chameleon and Vainshtein types, the modification to GR is strongest in low-density regions, making voids a promising tool to constrain them. In this paper, we have demonstrated for a specific example that this is indeed true. Voids as a probe for cosmology have until very recently been considered as degraded by the ambiguities in the void definitions and void-finding algorithms. For example, Colberg et al. (2005) showed that different void finders do not agree even on the void abundances. Also, even applied on the same data set, different void-finding algorithms can output very different void density profiles (see for examples, Pan et al. 2012; Nadathur et al. 2015, where the latter group, using the tessellation-based code ZOBOV (Neyrinck et al. 2005), obtained significantly shallower void density profiles than what the former group found using a spherical underdensity algorithm. This is because watershed methods such as ZOBOV tend to find voids that are irregularly shaped, but the density profiles are measured by spherical averaging, which smears out void edges and makes voids profiles shallower. Spherical voids are very different, and have steep density profiles as we have discussed in the above.). However, as a void-finding algorithm is only a way to measure and quantify the distribution of dark matter, or its tracers such as galaxies and galaxy clusters, the details of the algorithm itself are less relevant as long as one uses the same algorithm to find voids in the mock universe (i.e. simulations) and the real one. It can be envisaged that our results might change quantitatively if we use watershed methods to find voids. In this paper, we choose to use spherical voids partly because they have the advantage of having steep density profiles; the steep density profiles can lead to a stronger lensing tangential shear signal, which is beneficial for observations. On the other hand, if one takes irregularly shaped voids and spherical averaging over them, the mean density profile will be shallower, while at the same time the averaged fifth force in each spherical shell may be weaker because high-density regions (where the chameleon screening is strong) are included. The lensing signal may also be diluted.

Indeed, although often considered as a disadvantage, the ambiguity of defining and identifying voids can also have positive consequences: even if one void-finding algorithm is not sensitive to the modifications of gravity, others may well be, and by trying different algorithms one can hopefully find the optimal one to constrain a given type of gravity theory. For example, when determining the radius of a void, we have tried two different methods: (1) we divide particles around prospective void centres into a number of bins, find the bin at which the accumulative density first exceeds $\Delta_{\rm void}$, and let the void radius equal the radius of this bin; (2) not using the binning, but instead calculating the cumulative density every time when the void finder encounters another particle (or tracer), stopping when it first exceeds $\Delta_{\rm void}$, and taking the void radius as the distance between that particle and the void centre. Because of the

sparseness of tracers in empty regions, we have found that the two methods can lead to different halo number density profiles, though the significant levels of deviation from GR and the dark matter density profiles (hence lensing signals) are stable. The study and comparison with other void-finding algorithms is beyond the scope of this paper and will be left for future work.

Our results above have important implications for cosmological tests of gravity. It is often believed that cosmology can only place loose constraints on chameleon-type modified gravity theories, such as $f(R)$ gravity (see for example, Lombriser 2014, for a recent review). Here, we see that void abundances, the stacking of void profiles and tangential shears and velocity profiles, can put constraints almost as strong as those from astrophysical tests, which suffer from bigger uncertainties. As such, it points out a new powerful probe which can potentially be applied to other types of gravity theories as well. A recent study for Dvali-Gabadadze-Poratti (DGP) model has pointed out that the fifth forces are screened (via the Vainshtein screening) in haloes, but not in voids, filaments and walls (Falck et al. 2014). This suggest that voids may also be powerful to probe modified gravity models with Vainshtein screening.

## ACKNOWLEDGEMENTS

We thank Jiaxin Han, Marius Cautun, Pablo Arnalte-Mur, Shaun Cole, Carlos Frenk, Simon White, Rien van de Weygaert, Sergei Shandarin and John Peacock for helpful discussions and comments. YC is supported by the Durham Junior Research Fellowship. NP acknowledges support by Fondecyt Regular No. 1110328 and BASAL PFB-06 CATA. BL is supported by the Royal Astronomical Society and Durham University. YC and BL also acknowledge a grant with the RCUK reference ST/F001166/1. NP acknowledges support by the European Commission's Framework Programme 7, through the Marie Curie International Research Staff Exchange Scheme LACEGAL (PIRSES-GA-2010-269264).

The simulations and part of data analysis for this paper were performed using the DiRAC Data Centric system at Durham University, operated by the Institute for Computational Cosmology on behalf of the STFC DiRAC HPC Facility (http://www.dirac.ac.uk). This equipment was funded by BIS National E-infrastructure capital grant ST/K00042X/1, STFC capital grant ST/H008519/1, and STFC DiRAC Operations grant ST/K003267/1 and Durham University. DiRAC is part of the National E-Infrastructure. Part of the analysis was done on the Geryon cluster at the Centre for Astro-Engineering UC, which received recent funding from QUIMAL 130008 and Fondequip AIC-57. Access to the simulations used in this paper can be obtained from the authors.

## REFERENCES

Achitouv I., Neyrinck M., Paranjape A., 2013, preprint (arXiv:1309.3799)
Albrecht A. et al., 2006, preprint (astro-ph/0609591)
Amendola L., Frieman J. A., Waga I., 1999, MNRAS, 309, 465
Anderson L. et al., 2014, MNRAS, 441, 24
Arnold C., Puchwein E., Springel V., 2014, MNRAS, 440, 833
Bernstein G. M., Cai Y.-C., 2011, MNRAS, 416, 3009
Beutler F. et al., 2014, MNRAS, 443, 1065
Bos E. G., van de Weygaert R., Dolag K., Pettorino V., 2012, MNRAS, 426, 440
Bose S., Hellwing W. A., Li B., 2015, J. Cosmol. Astropart. Phys., 02, 034
Cai Y.-C., Bernstein G., 2012, MNRAS, 422, 1045
Cai Y.-C., Neyrinck M. C., Szapudi I., Cole S., Frenk C. S., 2013, ApJ, 786, 110
Cai Y.-C., Li B., Cole S., Frenk C. S., Neyrinck M., 2014, MNRAS, 439, 2978
Carroll S. M., De Felice A., Duvvuri V., Easson D. A., Trodden M., Turner M. S., 2005, Phys. Rev. D, 71, 063513
Ceccarelli L., Paz D., Lares M., Padilla N., Lambas D. G., 2013, MNRAS, 434, 1435
Clampitt J., Jain B., 2014, preprint (arXiv:1404.1834)
Clampitt J., Cai Y.-C., Li B., 2013, MNRAS, 431, 749
Colberg J. M., Sheth R. K., Diaferio A., Gao L., Yoshida N., 2005, MNRAS, 360, 216
Colberg J. M. et al., 2008, MNRAS, 387, 933
De Felice A., Tsujikawa S., 2010, Living Rev. Relativ., 13, 3
de Putter R., Doré O., Takada M., 2013, preprint (arXiv:1308.6070)
Falck B., Koyama K., Zhao G.-b., Li B., 2014, J. Cosmol. Astropart. Phys., 7, 58
Gaztañaga E., Eriksen M., Crocce M., Castander F. J., Fosalba P., Marti P., Miquel R., Cabré A., 2012, MNRAS, 422, 2904
Granett B. R., Neyrinck M. C., Szapudi I., 2008, ApJ, 683, L99
Hamaus N., Sutter P. M., Wandelt B. D., 2014, Phys. Rev. Lett., 112, 251302
Hellwing W. A., Barreira A., Frenk C. S., Li B., Cole S., 2014, Phys. Rev. Lett., 112, 221102
Higuchi Y., Oguri M., Hamana T., 2013, MNRAS, 432, 1021
Hotchkiss S., Nadathur S., Gottlöber S., Iliev I. T., Knebe A., Watson W. A., Yepes G., 2015, MNRAS, 446, 1321
Hu W., Sawicki I., 2007, Phys. Rev., D, 76, 064004
Ilić S., Langer M., Douspis M., 2013, A&A, 556, A51
Jennings E., Baugh C. M., Li B., Zhao G.-B., Koyama K., 2012, MNRAS, 425, 2128
Jennings E., Li Y., Hu W., 2013, MNRAS, 434, 2167
Khoury J., Weltman A., 2004, Phys. Rev. Lett., 93, 171104
Kirk D., Lahav O., Bridle S., Jouvel S., Abdalla F. B., Frieman J. A., 2013, preprint (arXiv:1307.8062)
Knollmann S. R., Knebe A., 2009, ApJ, 182, 608
Krause E., Chang T.-C., Doré O., Umetsu K., 2013, ApJ, 762, L20
Lam T. Y., Nishimichi T., Schmidt F., Takada M., 2012, Phys. Rev. Lett., 109, 051301
Lam T. Y., Clampitt J., Cai Y.-C., Li B., 2015, MNRAS, 450, 3319
Laureijs R. et al., 2011, preprint (arXiv:1110.3193)
Lavaux G., Wandelt B. D., 2012, ApJ, 754, 109
Li B., 2011, MNRAS, 411, 2615
Li B., Barrow J. D., 2011, Phys. Rev., D, 83, 024007
Li B., Efstathiou G., 2012, MNRAS, 421, 1431
Li B., Zhao G., Teyssier R., Koyama K., 2012a, J. Cosmol. Astropart. Phys., 01, 051
Li B., Zhao G.-B., Koyama K., 2012b, MNRAS, 421, 3481
Li B., Hellwing W. A., Koyama K., Zhao G.-B., Jennings E., Baugh C. M., 2013, MNRAS, 428, 743
Lombriser L., 2014, Annalen der Physik, 526, 259
McDonald P., Seljak U., 2009, J. Cosmol. Astropart. Phys., 10, 7
Martino M. C., Sheth R. K., 2009, preprint (arXiv:0911.1829)
Melchior P., Sutter P. M., Sheldon E. S., Krause E., Wandelt B. D., 2014, MNRAS, 440, 2922
Nadathur S., Hotchkiss S., Diego J. M., Iliev I. T., Gottlöber S., Watson W. A., Yepes G., 2015, MNRAS, 449, 3997
Neyrinck M. C., Gnedin N. Y., Hamilton A. J. S., 2005, MNRAS, 356, 1222
Padilla N. D., Ceccarelli L., Lambas D., 2005, MNRAS, 363, 977 (P05)
Pan D. C., Vogeley M. S., Hoyle F., Choi Y.-Y., Park C., 2012, MNRAS, 421, 926
Paranjape A., Lam T. Y., Sheth R. K., 2011, MNRAS, 420, 1648
Paz D., Lares M., Ceccarelli L., Padilla N., Lambas D. G., 2013, MNRAS, 436, 3480
Peebles P. J. E., 2001, ApJ, 557, 495
Peebles P. J. E., Nusser A., 2010, Nature, 465, 565
Planck Collaboration XIX 2014, A&A, 571, 19
Ricciardelli E., Quilis V., Varela J., 2014, MNRAS, 440, 601
Sánchez A. G. et al., 2014, MNRAS, 440, 2692
Schmidt F., Vikhlinin A., Hu W., 2009, Phys. Rev., D, 80, 083505
Sheth R. K., van de Weygaert R., 2004, MNRAS, 350, 517

Sotiriou T. P., Faraoni V., 2010, Rev. Mod. Phys., 82, 451
Sutter P. M., Carlesi E., Wandelt B. D., Knebe A., 2015, MNRAS, 446L, 1
Sutter P. M., Pisani A., Wandelt B. D., Weinberg D. H., 2014a, MNRAS, 443, 2983
Sutter P. M., Lavaux G., Wandelt B. D., Weinberg D. H., Warren M. S., 2014b, MNRAS, 438, 3177
Tikhonov A. V., Klypin A., 2009, MNRAS, 395, 1915
Tinker J. L., Conroy C., 2009, ApJ, 691, 633
Vainshtein A. I., 1972, Phys. Lett. B, 39, 393
Xie L., Gao L., Guo Q., 2014, MNRAS, 441, 933
Zehavi I. et al., 2011, ApJ, 736, 59

This paper has been typeset from a TEX/LATEX file prepared by the author.